Monte Carlo prediction of the energy performance of a photovoltaic panel using detailed meteorological input data

Thomas Villemin, Olivier Farges, Gilles Parent, Rémy Claverie

Monte Carlo prediction of the energy performance of a photovoltaic panel using detailed meteorological input data

Thomas Villemin [a,b,*], Olivier Farges [a], Gilles Parent [a], Rémy Claverie [b]

[a] Université de Lorraine, CNRS, LEMTA, F-54000 Nancy, France
[b] Cerema Est, TEAM Research Group, 71 rue de la grande haie F-54510 Tomblaine, France

ARTICLE INFO

Keywords:
Photovoltaics
Monte Carlo method
Heat transfers
Renewable technologies

ABSTRACT

Modeling the thermal behavior of a photovoltaic system is one step toward a better simulation of its electrical performances. In this study, a numerical model of the energy balance of a 310 W photovoltaic panel is developed and used to estimate the panel's temperature by integrating the meteorological parameters over time. The input factors are the global irradiance, wind speed, ambient temperature, ground and sky temperatures if available. The energy balance is interpreted in a probabilistic way using the Monte Carlo method which provides access to an estimation of the system temperature at any probe location. This estimation is validated using experimental data for typical days with clear, cloudy and rainy conditions. Then the model is used to determine the electrical production. Firstly, it is used for the month of June 2022 where the energy estimate is compared to the experimental measurements in Nancy (France). Secondly, the model is applied over the year 2019 for two different locations — in Nancy (France) and in Las Vegas (Nevada, USA). The results are analyzed and compared with the European photovoltaic simulation tool PVGIS. Finally, the electrical production in Nancy from 2013 to 2020 is estimated using the present model.

1. Introduction

Over the past few decades, the installation of photovoltaic panels (PV panels) has accelerated dramatically and these technologies will play an important role in tomorrow's energy mix. In 2021, the cumulative installed solar capacity worldwide was approximately 840 GW [1] and the trend is moving upwards. This is due to the reduction of cell manufacturing costs and the improvement of their electrical efficiency. The electrical efficiency is generally between 10 % and 20 % for most of the PV panels available on the market with a record efficiency in laboratory of 26.7 % [2,3] for a silicon-based technology. A typical monocrystalline silicon panel is composed of five layers — photovoltaic cells made of silicon which are encased in two EVA layers, a front layer of glass and a plastic back sheet for the rear-ground facing side. The total thickness of these five layers is generally between 3 mm to 5 mm.

One phenomenon that has been well referenced in the literature is the decrease of the electrical efficiency with the increase of the panel temperature [4,5]. Yet, part of the incident solar radiation is not converted into electrical energy and contributes to the heating of the panel and the temperature of the panel is the result of a complex interaction between the panel and its environment — intermittence of solar radiation, random fluctuations of the wind, precipitation [6]. Despite this, photovoltaic technologies are certified under Standard Test Conditions (STC) corresponding to an ideal situation involving incident solar radiation of 1000 W m^{-2} under AM 1.5 conditions (solar spectrum with an angle of incidence of 48° in relation to the zenith) and a cell temperature of 25 °C. However it has been shown in the literature that these Standard Test Conditions are very seldom encountered in real operation configurations around the world [7]. Despite this, one of the most commonly used equations to determine the efficiency of a panel as a function of temperature depends on two parameters derived from STC and will be exploited and presented later in this article. In general, the datasheet of the PV module provides the values of the efficiency (η_{ref}) and temperature coefficient for STC (β_{ref}). As a result of this dependence between electrical production and panel's operating temperature, clearly an effective evaluation of the thermal behavior of the PV system is crucial to determine its electrical production depending on the location, environmental conditions and mounting configurations [8]. Another topic has emerged in recent years concerning the cooling issue of photovoltaic panels. To reduce the thermal stress over the lifespan of the panel and enhance the electrical production, cooling techniques have become essential and more and more studies are focusing on this point [9]. Cooling can be passive or active but for all situations it involves thermal transfers and would

* Corresponding author at: Université de Lorraine, CNRS, LEMTA, F-54000 Nancy, France.
E-mail address: thomas.villemin@univ-lorraine.fr (T. Villemin).

Nomenclature

β_{pv}	PV panel temperature coefficient (% K^{-1})
Δt	temporal step for the implicit FDM (s)
Δz	spatial step for the implicit FDM (m)
δ	conductive random walk step (m)
δ_r	re-injection step conductive random walk step (m)
ϵ	PV panel emissivity
η_{pv}	PV panel electrical efficiency (%)
λ	PV panel heat conductivity (W m^{-1} K^{-1})
∂D_b	bottom domain boundary
∂D_u	upper domain boundary
$\mathcal{D}$	solid domain of the PV panel
$\mathcal{H}$	Heaviside step function
$\mathcal{S}$	source term (W m^{-3})
Nu	Nusselt number
Pr	Prandtl number
Ra	Rayleigh number
Re	Reynolds number
SR	soiling ratio
ν	frequency (Hz)
∂D	boundary of the solid domain of the PV panel
ϕ_u^s	global solar irradiance (W m^{-2})
ϕ_{cd}	conductive heat flux (W m^{-2})
ϕ_{cv}	convective heat flux (W m^{-2})
$\phi_{\text{LW}}^{\downarrow}$	downward longwave radiation (W m^{-2})
ϕ_{rad}	radiative heat flux (W m^{-2})
ρ	PV panel density (kg m^{-3})
ρ_{front}	PV panel reflectivity of the front surface
σ	standard deviation
σ_{SB}	Stefan–Boltzmann constant (W m^{-2} K^{-4})
Θ	random variable of temperature
θ	tilt angle of the panel (°)
θ_i	realization of the random variable Θ (K)
$\mathbf{x}$	position in the domain
$\mathbf{n}$	normal to the surface
$\boldsymbol{\omega}$	sampled direction in conductive random walk
A_{pv}	PV panel surface (m^2)
C_D	surface drag coefficient
C_p	PV panel heat capacity (J kg^{-1} K^{-1})
$C_{10-2.5}$	concentration of PM 10 (kg m^{-3})
$C_{2.5}$	concentration of PM 2.5 (kg m^{-3})
h_{cv}	convective heat transfer coefficient (W K^{-1} m^{-2})
h_{rad}	radiative heat transfer coefficient (W K^{-1} m^{-2})
l	lateral
L_c	characteristic length of the PV panel (m)
$L_{\nu,\boldsymbol{\omega}}$	luminance (W m^{-2} Hz^{-1} sr^{-1})
$L_{\nu,\boldsymbol{\omega}}^{eq}$	luminance at equilibrium (W m^{-2} Hz^{-1} sr^{-1})
M	number of spatial nodes for the implicit FDM
m	mass accumulation of dust (kg m^{-2})
N_{mc}	number of Monte Carlo realizations
r_a	aerodynamic resistance (s m^{-1})
t	time (s)
$T(\mathbf{x}, t)$	temperature of the PV panel (K)
T_I	initial temperature (K)
T_{air}	air temperature (K)
T_{ref}	reference temperature for STC (K)
T_{sky}	sky temperature (K)
$T_{R,\boldsymbol{\omega},\nu}$	brightness temperature (K)
U	wind speed at 10 m (m s^{-1})
$u^\star$	friction velocity (m s^{-1})
v_d	deposition velocity (m s^{-1})
v_s	settling velocity resistance (m s^{-1})
V_{pv}	PV panel volume (m^3)
w	cumulative mass of dust (kg m^{-2})

b	bottom
u	up

require significantly better understanding of the energy balance of such technologies [10–13].

To study this question, two complementary study directions are possible namely experimental and numerical studies. Most work has been numerical in nature and has focused on the thermal or the electrical evaluation of the PV panel. Skoplaki and Gaglia [14,15] have developed direct empirical correlations to express electrical efficiency as a function of the operating temperature and demonstrated that the decay of the electrical production is linear with increasing panel temperature. These types of models have also been developed and assessed in [16–18]. However, these approaches are very often limited to the situations in which they have been established and would require caution when directly applying them to other locations and situations.

In order to avoid these pitfalls, a thermal model of a photovoltaic panel must be able to temporally integrate meteorological variables to correctly simulate the different thermal exchanges (radiative, convective, conductive exchanges). These parameters are very variable by nature which leads to complex thermal dynamics within the panel [19]. Many models presented in the literature use finite elements or finite differences [20,21] to solve the optical, electrical and thermal models with similar simplifications for most of them. As an example, the ground temperature is often taken as the ambient temperature. These models often face geometric problems and solve the heat balance in 1D or 2D. Some models have been developed in 3D but this in turn brings up computational time problems when they are used to estimate the electrical production over a long period [22]. This is why the vast majority of the numerical models are developed in 1D and limited to the estimation of the panel temperature. Other drawbacks in several models are the absence of thermal capacity in the panel and the resolution of the thermal balance with a quasi steady-state approach whereas it was clearly demonstrated in [23,24] that a PV panel has a non-negligible thermal inertia. The model developed by Sandia National Laboratories [25] is widely used in the photovoltaic community to estimate the module performance. This model requires more than 10 parameters to draw the current–voltage characteristics and several parameters need to be evaluated experimentally which is not always possible. Moreover, the heat capacity of the PV panel in their thermal model (SAPM1) is neglected which leads to sudden variations in PV panel temperature depending on weather conditions. Other parameters affecting panel production are very rarely discussed and/or considered in these models, for example the aging of the panel

materials over the panel's lifetime (about 25 years for a typical commercial technology [26]), dust deposition over time if the panel is not cleaned sufficiently, electrical losses in the cables from the micro-inverter (Direct Current – DC – circuit) to Alternative Current grid, etc.

Finally, these models are mostly validated on a temperature profile obtained experimentally on a single given day [27]. It should be kept in mind that the initial objective is to estimate the energy performance of the panel over its lifetime (about 25 years). The proposed model based on the Monte-Carlo method has many advantages including handling the 3D geometrical complexity of the panel and its environment without restricting the possibility to evaluate electrical production over a large period of time by integrating physical effects at different spatial scales in a transient simulation [28–30]. In this work, a model of the thermal balance of a 310 W PV panel is presented with a similar approach to that proposed in the literature but the fact that it also integrates this original method of resolution means the model can go beyond the stage of purely thermal validation to address energy problems on larger time scales including different effects such as soiling.

In Section 2, the Monte Carlo method is presented and validated in a simple configuration case in Section 2.2. The model is also presented for a photovoltaic panel in Section 2.3. Then in Section 3 the model is validated for two experimental conditions — firstly for controlled conditions in Section 3.2 where the high variability of the meteorological parameters is avoided and secondly for outdoor configuration in Section 3.3 with experimental data from Cerema (Nancy, France) facilities. Finally, the model is exploited to estimate monthly and annual electrical production for two different locations in Section 3.4.

2. Methods

In this section, the principles of the Monte Carlo method are introduced and then details are given of the model describing the heat equation of the photovoltaic panel and its resolution. For the reader interested in more information about this section, the theoretical framework is described with more details in [31].

2.1. Monte Carlo method

The Monte Carlo method is a statistical method consisting in estimating a physical quantity as the expectation of a random variable. More specifically, this is possible when the quantity under study is written in the form of an integral. In this paper, the physical quantity of interest is the temperature of the panel at a position $\mathbf{x}$ and a time t. This temperature is expressed as the expectation of the random variable $\Theta(\mathbf{x},t)$:

$$\overline{T}(\mathbf{x},t) = \mathbb{E}\left[\Theta(\mathbf{x},t)\right] \approx \frac{1}{N_{\text{mc}}}\sum_{i=1}^{N_{\text{mc}}}\theta_i \tag{1}$$

θ_i is a realization of the random variable Θ. A realization consists in the construction of a random path starting at position $\mathbf{x}$ and time t. This random path stops when the initial condition or a known temperature is reached. For each realization, a temperature is retained. The estimation of the temperature at the considered starting point consists in averaging all the realizations.

2.1.1. Monte Carlo path for conductive heat transfer

The transient heat equation is solved inside the PV panel according to Eq. (2).

$$\rho C_p \frac{\partial T(\mathbf{x},t)}{\partial t} = \lambda \nabla^2 T(\mathbf{x},t) + S(\mathbf{x},t) \tag{2}$$

where $S(\mathbf{x},t)$ is the source term (W m^{-3}). As classically established when moving from a deterministic expression to a stochastic formalism [31], the laplacian of the temperature with finite differences Eq. (3) is obtained. For the sake of completeness, several discretization schemes could be applied to the laplacian operator as detailed in [32].

$$\begin{aligned}\frac{\partial T(\mathbf{x},t)}{\partial t} &= \frac{\lambda}{\rho C_p \delta^2}\left(T(\mathbf{x}\pm\delta\mathbf{e_x},t)+T(\mathbf{x}\pm\delta\mathbf{e_y},t)\right.\\ &\quad\left.+\ T(\mathbf{x}\pm\delta\mathbf{e_z})-6T(\mathbf{x},t)\right)+S(\mathbf{x},t)\\ &= -\alpha\left[T(\mathbf{x},t)-\left(T^\star(\mathbf{x},t)+\frac{\delta^2}{6\lambda}S(\mathbf{x},t)\right)\right]\end{aligned} \tag{3}$$

with $T^\star(\mathbf{x},t) = \frac{1}{6}\left(T(\mathbf{x}\pm\delta\mathbf{e_x},t)+T(\mathbf{x}\pm\delta\mathbf{e_y},t)+T(\mathbf{x}\pm\delta\mathbf{e_z})\right)$ and $\alpha = \frac{6\lambda}{\rho C_p\delta^2}$.

As the coordinate system made with the basis $(\mathbf{e_x},\mathbf{e_y},\mathbf{e_z})$ can be chosen arbitrarily, the temperature $T^\star(\mathbf{x},t)$ can be seen at each random step as the average temperature on the sphere centered on $\mathbf{x}$ and with a radius δ. Therefore, let us note $T^\star(\mathbf{x},t) = \int_{4\pi} \mathrm{d}\boldsymbol{\omega} p_{\boldsymbol{\Omega}}(\boldsymbol{\omega}) T(\mathbf{x}+\delta\boldsymbol{\omega},t)$ where $\boldsymbol{\omega}$ is the sampled direction according to the probability density function $p_{\boldsymbol{\Omega}}(\boldsymbol{\omega}) = \frac{1}{4\pi}$.

Using the Duhamel's formula, the expression of the temperature from Eq. (3) is given by Eq. (4):

$$\begin{aligned}T(\mathbf{x},t) = \int_0^{+\infty}\mathrm{d}\tau p_{\mathcal{T}}(\tau)\left[\mathcal{H}(\tau-t)T_I(\mathbf{x})+\mathcal{H}(t-\tau)\right.\\ \left.\left[T^\star(\mathbf{x},t-\tau)+\frac{\delta^2}{6\lambda}S(\mathbf{x},t-\tau)\right]\right]\end{aligned} \tag{4}$$

where $p_{\mathcal{T}}(\tau) = \alpha\exp(-\alpha\tau)$ is an exponential probability density function whose parameter is $\alpha = \frac{6\lambda}{\rho C_p\delta^2}$ and $T_I(\mathbf{x})$ is the temperature at the initial time $t_I = 0$.

Finally, Eq. (4) is reformulated with a probabilistic expression. A key point is the property of double randomization which means we can obtain a nested expectation of random variables but only one random path [33,34].

$$\begin{aligned}T(\mathbf{x},t) = \mathbb{E}\left[\mathcal{H}(\mathcal{T}-t)T_I(\mathbf{x})+\mathcal{H}(t-\mathcal{T})\left(\mathbb{E}\left[T^\star(\mathbf{x}+\delta\boldsymbol{\Omega},t-\mathcal{T})\right]\right.\right.\\ \left.\left.+\ \frac{\delta^2}{6\lambda}S(\mathbf{x},t-\mathcal{T})\right)\right]\end{aligned} \tag{5}$$

where $\mathcal{T}$ obeys an exponential law in the interval $]0,+\infty[$ with parameter $\alpha = \frac{6\lambda}{\rho C_p\delta^2}$ and $\boldsymbol{\Omega}$ follows a uniform sampling on unit hemisphere at the surface ($p_{\boldsymbol{\Omega}}(\boldsymbol{\omega})$).

The Monte Carlo algorithm corresponding to Eq. (5) is detailed in Algorithm 1. In this algorithm, the variable C is an accumulator term taking into account any surface flux. In our photovoltaic application, this flux will be the global solar flux at the front surface of the PV panel.

Algorithm 1: Description of the Monte Carlo algorithm for the conductive path

```
Initialize C = 0
while t > t_I do
    Sample τ according to p_T
    t = t − τ
    if t < t_I then
        w = T(x, t_I) + C
    else
        Sample ω according to p_Ω
        x = x + δω
        C = C + (δ²/6λ) S(x, t)
```

2.1.2. Monte Carlo path at the boundaries

When the conductive path reaches one of the boundaries of the domain, the path has to be reformulated to couple the conductive, convective and radiative heat transfers.

The position at the boundary is denoted by $\mathbf{y}$. The equation of continuity of fluxes at $\mathbf{y}$ applies and is given by Eq. (6). In what follows, $\boldsymbol{\omega}$ is uniformly sampled on the unit hemisphere at the surface at $\mathbf{y}$ and

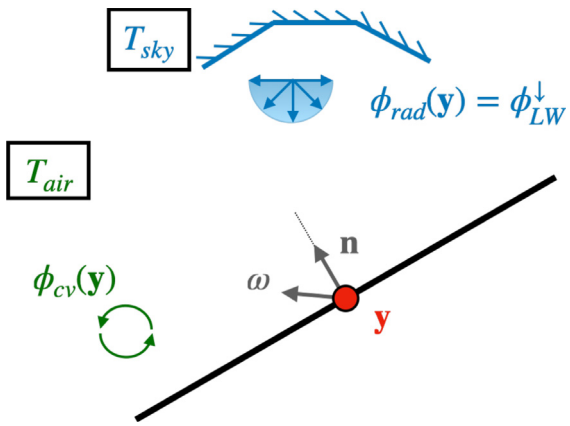

Fig. 1. Continuity equation at the boundaries of the PV panel domain. T_{sky} and T_{air} are the air and sky temperatures respectively. $\phi^{\downarrow}_{LW}$ is the long wave radiation. The radiative and convective fluxes at position $\mathbf{y}$ are denoted $\phi_{\text{rad}}(\mathbf{y})$ and $\phi_{\text{cv}}(\mathbf{y})$ respectively.

$-\boldsymbol{\omega}$ is the direction in the opposite direction (incident to the surface). The situation is presented in Fig. 1.

$$\begin{aligned}&\phi_{\text{cd}}(\mathbf{y}) = \phi_{\text{cv}}(\mathbf{y}) + \phi_{\text{rad}}(\mathbf{y})\\ &\iff -\lambda \nabla T(\mathbf{y}) \cdot \mathbf{n} = \phi_{\text{cv}}(\mathbf{y}) + \int_{2\pi} \mathrm{d}\boldsymbol{\omega} \int_0^{\infty} \mathrm{d}\nu\, \epsilon \left(L^{eq}_{\nu,\boldsymbol{\omega}}(\mathbf{y}) - L_{\nu,-\boldsymbol{\omega}}(\mathbf{y}) \right) |\boldsymbol{\omega} \cdot \mathbf{n}|\end{aligned} \tag{6}$$

where $\mathbf{n}$ is the normal vector to the surface at the boundary point $\mathbf{y}$.

Using the brightness temperature $T_{R,\boldsymbol{\omega},\nu}(\mathbf{y})$, it is possible to express the intensity $L_{\nu,\boldsymbol{\omega}}(\mathbf{y})$ as Eq. (7).

$$L^{eq}_{\nu,\boldsymbol{\omega}}(\mathbf{y}) = L^{eq}_{\nu}(T_{R,\boldsymbol{\omega},\nu}(\mathbf{y})) = L_{\nu,\boldsymbol{\omega}}(T(\mathbf{y})) \tag{7}$$

Then, the intensity at equilibrium can be linearized around a reference temperature T_{ref} according to Eq. (8).

$$L^{eq}_{\nu}(T(\mathbf{y})) \approx L^{eq}_{\nu}(T_{\text{ref}}) + \left.\frac{\partial L^{eq}_{\nu}}{\partial T}\right|_{T_{\text{ref}}} (T_{R,\boldsymbol{\omega},\nu}(\mathbf{y}) - T_{\text{ref}}) \tag{8}$$

Considering that the void space between the surface of the panel and the surroundings is a transparent medium and that surroundings are black, the incident intensity is expressed as Eq. (9).

$$L_{\nu,-\boldsymbol{\omega}}(\mathbf{y}) = L^{eq}(T_{R,-\boldsymbol{\omega},\nu}) = L^{eq}_{\nu}(T_{\text{ref}}) + \left.\frac{\partial L^{eq}_{\nu}}{\partial T}\right|_{T_{\text{ref}}} (T_{R,-\boldsymbol{\omega},\nu} - T_{\text{ref}}) \tag{9}$$

Finally Eq. (6) is now expressed as Eq. (10).

$$\phi_{\text{cd}}(\mathbf{y}) = \phi_{\text{cv}}(\mathbf{y}) + \int_{2\pi} \mathrm{d}\boldsymbol{\omega} \int_0^{+\infty} \mathrm{d}\nu \left.\frac{\partial L^{eq}_{\nu}}{\partial T}\right|_{T_{\text{ref}}} \left(T(\mathbf{y}) - T_{R,-\boldsymbol{\omega},\nu}\right) \tag{10}$$

The final step is to reformulate Eq. (10) with a probabilistic expression as shown as in Eq. (11).

$$\phi_{\text{cd}}(\mathbf{y}) = \phi_{\text{cv}}(\mathbf{y}) + h_{\text{rad}} \left[T(\mathbf{y}) - \int_{2\pi} \mathrm{d}\boldsymbol{\omega}\, p_{\boldsymbol{\Omega}}(\boldsymbol{\omega}) \int_0^{+\infty} \mathrm{d}\nu\, p_{\mathcal{N}}(\nu) T_{R,-\boldsymbol{\omega},\nu} \right] \tag{11}$$

where $h_{\text{rad}} = 4\epsilon\sigma_{\text{SB}} T^3_{\text{ref}}$ is the radiative coefficient. The conductive ($\phi_{\text{cd}}(\mathbf{y})$) and convective ($\phi_{\text{cv}}(\mathbf{y})$) fluxes have to be expressed to obtain the final expression of the probabilized temperature at the boundary point $\mathbf{y}$. The conductive flux is simply expressed by approximating the gradient with a finite difference approach Eq. (12).

$$\phi_{\text{cd}}(\mathbf{y}) = -\lambda \nabla T(\mathbf{y}) \cdot \mathbf{n} \approx -\lambda \frac{T(\mathbf{y}) - T(\mathbf{y} - \delta_r \mathbf{n})}{\delta_r} \tag{12}$$

where δ_r is the re-injection step at the boundary. In general the re-injection step is chosen differently from δ.

For the convective flux, the description with a convective exchange coefficient h_{cv} and the temperature gradient between the air and the surface is used (Eq. (13)).

$$\phi_{\text{cv}}(\mathbf{y}) = h_{\text{cv}}(\mathbf{y})(T(\mathbf{y}) - T_{\text{air}}) \tag{13}$$

Finally, based on the assumption that the surrounding surfaces are gray or black, it is possible to express the temperature at the surface of the PV panel as a weighting of the different sources (conductive, convective, radiative) using a probabilistic point of view according to Eq. (14).

$$T(\mathbf{y}) = \mathbb{P}_{\text{cd}} T(\mathbf{y} - \delta_r \mathbf{n}) + \mathbb{P}_{\text{cv}} T_{\text{air}} + \mathbb{P}_{\text{rad}} \int_{2\pi} \mathrm{d}\boldsymbol{\omega}\, p_{\boldsymbol{\Omega}}(\boldsymbol{\omega}) T_{R,-\boldsymbol{\omega}} \tag{14}$$

$$\begin{cases} \mathbb{P}_{\text{cd}} = \dfrac{\lambda/\delta_r}{\lambda/\delta_r + h_{\text{cv}}(\mathbf{y}) + h_{\text{rad}}} \\ \mathbb{P}_{\text{cv}} = \dfrac{h_{\text{cv}}(\mathbf{y})}{\lambda/\delta_r + h_{\text{cv}}(\mathbf{y}) + h_{\text{rad}}} \\ \mathbb{P}_{\text{rad}} = \dfrac{h_{\text{rad}}}{\lambda/\delta_r + h_{\text{cv}}(\mathbf{y}) + h_{\text{rad}}} \end{cases} \tag{15}$$

$\mathbb{P}_{\text{cd}}$ is the probability to return to conduction after reaching the surface in $\mathbf{y}$. In this case, the random walk in the solid domain continues until a known temperature or the initial temperature is found. $\mathbb{P}_{\text{cv}}$ is the probability to go into convection and the air temperature is retained for the realization at the current time. Finally, $\mathbb{P}_{\text{rad}}$ is the probability for the random path to continue into radiation. In this case, the algorithm stops because the radiative temperatures (sky or ground temperatures) are also known from the weather data.

The solar flux must also be taken into account for the case of the front side of the PV panel. Each time the random walk reaches the front side of the PV panel, a variable (noted F in Algorithm 2 and initialized to zero at the beginning of every random path) is incremented by the quantity $\frac{\phi^s_u(t)}{\lambda/\delta_r + h_{\text{cv}}(\mathbf{y}) + h_{\text{rad}}}$. Then, this variable is added to the retained temperature of the random path. The final expression of the temperature at the boundary is given in Eq. (16). The corresponding Monte Carlo algorithm is given in Algorithm 2.

$$T(\mathbf{y}) = \mathbb{P}_{\text{cd}} T(\mathbf{y} - \delta_r \mathbf{n}) + \mathbb{P}_{\text{cv}} T_{\text{air}} + \mathbb{P}_{\text{rad}} \int_{2\pi} \mathrm{d}\boldsymbol{\omega}\, p_{\boldsymbol{\Omega}}(\boldsymbol{\omega}) T_{R,-\boldsymbol{\omega}} + \frac{\phi^s_u(t)}{\lambda/\delta_r + h_{\text{cv}}(\mathbf{y}) + h_{\text{rad}}} \tag{16}$$

Algorithm 2: Description of the Monte Carlo algorithm for the boundary condition (with accumulation term for the front side due to the solar irradiance)

```
if y ∈ ∂D then
    Sample r uniformly on [0, 1]
    C = C + φ^s_u(t) / (λ/δ_r + h_cv(y) + h_rad)
    if r < P_cd then
        y = y − δ_r n
    else if r < P_cd + P_cv then
        w = T_air + F (convective path)
    else
        Sample ω according to p_Ω(ω)
        w = T_{R,−ω} + C (radiative path)
```

2.1.3. Random walk technique for conductive path

The random walk was described in Section 2.1.1 and Section 2.1.2 for conductive path and flux continuity at the boundaries of the solid domain. The expressions derived in these two sections introduced two fixed parameters δ and δ_r that respectively correspond to the moving step at each displacement and the length of re-injection in the solid domain from one of the boundaries. The Monte Carlo algorithm converges to the exact solution when these two deterministic parameters tend to zero. Obviously, the smaller these two parameters are, the longer it takes for the algorithm to finish the calculation. As is the case for deterministic methods, a compromise between very fine step lengths and accuracy of the solution has to be determined. In this work, different values of δ and δ_r were tested until the solution no longer evolves with smaller steps.

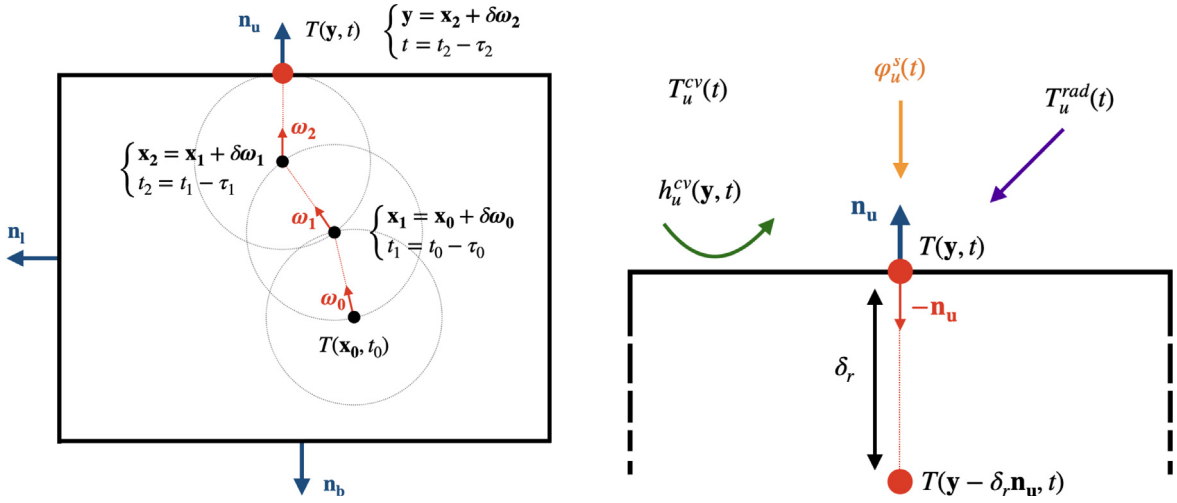

(a) Random walk in conduction according to the Walk on Sphere principle with constant step δ. The path started at point $\mathbf{x_0}$ at time t_0 and reached the upper surface at position $\mathbf{y}$ at time t.

(b) Continuity of heat fluxes at the upper interface. The temperature $T(\mathbf{y},t)$ is evaluated by superimposing the known temperatures and flows of the problem weighted by the probabilities associated with each of the events.

Fig. 2. Principle of the random walk in conduction and its behavior at interfaces.

Several techniques exist to construct the conductive random walk. The one used in this work is δ-sphere with constant δ. Each time a new position in the solid has to be evaluated, a random direction $\mathbf{u}$ is sampled and the retained moving step is calculated as $\delta = \min(\delta_{\text{wos}}, \delta_{\mathbf{u}}, \delta_{-\mathbf{u}})$ where $\delta_{\mathbf{u}}$ (resp. $\delta_{-\mathbf{u}}$) is the distance from the current location to the boundary in the direction of $\mathbf{u}$ (resp. in the direction of $-\mathbf{u}$). One example of the conductive walk is given in Fig. 2(a). The re-injection from the boundary is also illustrated in Fig. 2(b) with a re-injection step that is equal to δ_r. More details and explanations can be found about the moving steps and the conductive random walk in [31].

2.2. Validation of the Monte Carlo algorithm for an academic configuration

2.2.1. Description of the studied configuration

The Monte Carlo method was applied to a simplified one-dimensional transient heat balance case and compared to a finite difference method. The system consists of an opaque plate of thickness 0.0045 m inclined by 30° with respect to the horizontal. It is subjected to a heat flux on the front side and the system exchanges heat with the environment through convective and radiative transfers. On the front side, the plate is considered to exchange with the sky and with the ground on the back side which means the radiation temperatures are different and view factors are thus calculated for both sides.

The view factors are given in Eq. (17) where θ is the tilt angle of the PV panel with respect to the horizontal plane (i.e. the ground).

$$\begin{aligned} F_{\text{front}\to\text{sky}} &= \frac{1}{2}(1+\cos(\theta)) \\ F_{\text{front}\to\text{ground}} &= \frac{1}{2}(1-\cos(\theta)) \\ F_{\text{back}\to\text{sky}} &= \frac{1}{2}(1+\cos(\pi-\theta)) \\ F_{\text{back}\to\text{ground}} &= \frac{1}{2}(1-\cos(\pi-\theta)) \end{aligned} \tag{17}$$

In the Monte Carlo algorithm, the view factors are not calculated. Instead, when the random walk reaches front or back side of the PV panel, a unit vector is sampled around the normal direction. If this sampled vector is pointing toward the ground, the ground temperature is retained to compute the radiative coefficient, otherwise the sky temperature is chosen. With a large number of realizations this process is able to statistically represent the deterministic view factors introduced in Eq. (17).

The energy balance of the plane is given in Eq. (18) with heat equation inside the volume of the plane and the boundary conditions for the front and back sides.

$$\mathbf{x}\in D, t\in[t_I,t_F] : \rho C_p \frac{\partial T(\mathbf{x},t)}{\partial t} = -\boldsymbol{\nabla}\cdot(-\lambda\boldsymbol{\nabla}T(\mathbf{x},t)) \tag{18}$$

$$\mathbf{y}\in\partial D_u, t\in[t_I,t_F] : -\lambda\boldsymbol{\nabla}T(\mathbf{y},t)\cdot\mathbf{n_u} = \phi_u^{\text{cv}}(\mathbf{y},t)+\phi_u^{\text{rad}}(\mathbf{y},t)-\phi_u^s(t) \tag{19}$$

$$\mathbf{y}\in\partial D_b, t\in[t_I,t_F] : -\lambda\boldsymbol{\nabla}T(\mathbf{y},t)\cdot\mathbf{n_b} = \phi_b^{\text{cv}}(\mathbf{y},t)+\phi_b^{\text{rad}}(\mathbf{y},t) \tag{20}$$

$$\mathbf{x}\in D, t=t_I : T(\mathbf{x},t=t_I)=T_I(\mathbf{x}) \tag{21}$$

The 1-D finite difference model is implemented using the energy balance method with an implicit time scheme which allows any choice of time step.

2.2.2. Boundary nodes

The details are only presented for the front side of the plane but the final expression is similar for the back side except that there is no solar flux. The corresponding node is shown in Fig. 3 with label number 1. Temperatures at nodes 1 and 2 are denoted T_1 and T_2 respectively.

$$\rho C_p\frac{\Delta z}{2}\frac{T_1^{i+1}-T_1^i}{\Delta t} = \frac{\lambda}{\Delta z}(T_2^{i+1}-T_1^{i+1})+h_{\text{cv}}(T_{\text{air}}-T_1^{i+1})+h_{\text{rad}}(T_{\text{sky}}-T_1^{i+1})+\phi_u^s \tag{22}$$

$$T_1^{i+1}(1+\gamma\frac{\lambda}{\Delta z}+\gamma h_{\text{cv}})-\gamma\frac{\lambda}{\Delta z}T_2^{i+1} = \gamma h_{\text{cv}}T_{\text{air}}+\gamma\phi_u^s+T_1^i \tag{23}$$

with $\gamma=\frac{2\Delta t}{\rho C_p\Delta z}$ and i refers to the time step.

2.2.3. Inner nodes

The position of the corresponding nodes is shown in Fig. 3 with label number 2.

$$\rho C_p\Delta z\frac{T_j^{i+1}-T_j^i}{\Delta t} = \frac{\lambda}{\Delta z}(T_{j+1}^{i+1}-T_j^{i+1})+\frac{\lambda}{\Delta z}(T_{j-1}^{i+1}-T_j^{i+1}) \tag{24}$$

where the subscript j denotes the spatial coordinate. After some arrangements, the expression describing the temperature at node m and time $i+1$ is expressed in Eq. (25).

$$T_j^{i+1}(1+2\tau)-\tau(T_{j+1}^{i+1}+T_{j-1}^{i+1}) = T_j^i \tag{25}$$

with $\tau=\frac{\lambda\Delta t}{\rho C_p\Delta z^2}$.

The results from the implicit finite difference and Monte Carlo method are presented in Fig. 4. The initial temperature of the plate

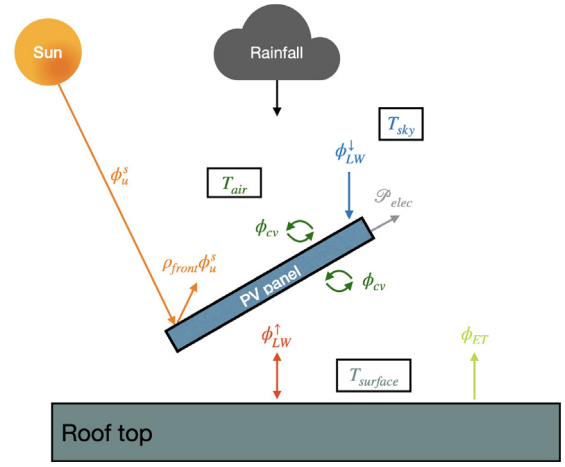

(a) The different heat transfers between the PV panel and its environment on a rooftop configuration.

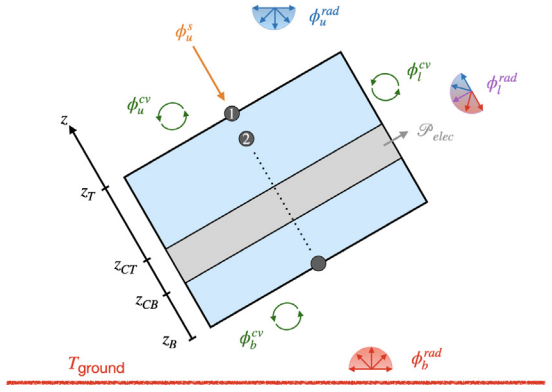

(b) Corresponding fluxes of the energy balance described in eqs. (26) to (30) with a zoom on the PV panel. The two different nodes described in the finite differences method are also displayed with corresponding indices.

Fig. 3. Schematic description of the heat and water exchanges between the PV panel and the environment. ϕ_{ET} represents the latent flux from the ground and is not directly considered in the model but is included in the measurement of the ground surface temperature under panel (T_{surface}).

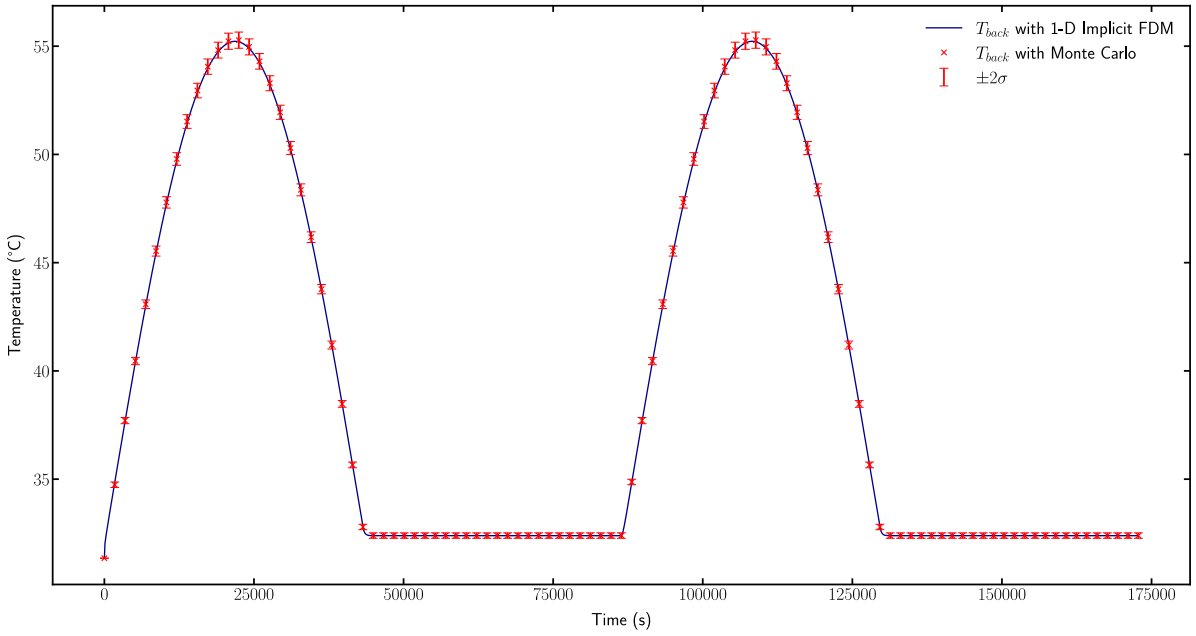

Fig. 4. Simulated T_{back} and comparison between the Implicit Finite Difference and Monte Carlo method. Each red cross corresponds to one Monte Carlo simulation with 20000 realizations.

is 304.5 K, air temperature is 303.15 K for the upper side and 313.15 K for the lower side, the incident irradiance has a time period of 48 h and its amplitude is 1000 W m^{-2}, the convective coefficients are 20 W K^{-1} m^{-2} and 10 W K^{-1} m^{-2} respectively for the upper and lower sides. The plate is tilted at 30° with respect to the horizontal.

2.3. Complete formulation of the MC algorithm to solve the thermal balance of the photovoltaic panel

The objective of the 3D model is to estimate the temperature of the photovoltaic panel (expected to be between −10 °C and 80 °C) at any given probe point by integrating the meteorological parameters. This model is then used to obtain an estimate of the electrical production over a full year.

2.3.1. Energy balance of the photovoltaic panel

The PV temperature $T(\mathbf{x},t)$ is the transient solution of the heat equation. The heat transfers are coupled at the boundaries of the solid domain of the PV panel. The heat equation and the different boundary conditions are presented in Eqs. (26) to (30). The situation of the panel in its environment with the representation of the different fluxes is shown in Fig. 3(a).

$$\mathbf{x} \in D, t \in [t_I, t_F] : \rho c_p \frac{\partial T(\mathbf{x},t)}{\partial t} = -\boldsymbol{\nabla} \cdot (-\lambda \boldsymbol{\nabla} T(\mathbf{x},t)) + \mathcal{S}_{\text{cells}}(\mathbf{x},t) \quad (26)$$

$$\mathbf{y} \in \partial D_u, t \in [t_I, t_F] : -\lambda \boldsymbol{\nabla} T(\mathbf{y},t) \cdot \mathbf{n_u} = \phi^{\text{cv}}_u(\mathbf{y},t) + \phi^{\text{rad}}_u(\mathbf{y},t) - \phi^{s}_u(t) \quad (27)$$

$$\mathbf{y} \in \partial D_b, t \in [t_I, t_F] : -\lambda \boldsymbol{\nabla} T(\mathbf{y},t) \cdot \mathbf{n_b} = \phi^{\text{cv}}_b(\mathbf{y},t) + \phi^{\text{rad}}_b(\mathbf{y},t) \quad (28)$$

$$\mathbf{y} \in \partial D_l, t \in [t_I, t_F] : -\lambda \boldsymbol{\nabla} T(\mathbf{y},t) \cdot \mathbf{n_l} = \phi^{\text{cv}}_l(\mathbf{y},t) + \phi^{\text{rad}}_l(\mathbf{y},t) \quad (29)$$

$$\mathbf{x} \in D, t = t_I : T(\mathbf{x}, t = t_I) = T_I(\mathbf{x}) \quad (30)$$

Table 1
Thermal and dimensional properties of the photovoltaic panel. The measurements were carried out at the LEMTA and represent the global thermal properties of the panel.

λ (W m^{-1} K^{-1})	ρ (kg m^{-3})	C_p (J kg^{-1} K^{-1})	ϵ_{front}	ϵ_{back}	A (m^2)	e (mm)
0.5	2500	813	0.91	0.92	1.64	4.5

The source term S_{cells} only occurs when $\mathbf{x}$ is in the silicon layer. In all other layers, this term is null. The thermal properties of the panel (ρ, λ, C_p) correspond to the properties of a homogeneous medium equivalent to all the layers and were measured at the LEMTA which is one of the main assumptions of the proposed model. The values for ρ, λ and C_p are provided in Table 1.

2.3.2. Heat sources

In this model and from a thermal point of view, the solar flux is considered in the front side of the PV panel and not as a radiative source appearing in volume in the different layers of the system as the medium is supposed to be opaque. The conversion of part of the solar radiation into electricity results in a lowering of the panel temperature. This source term is introduced in the energy balance according to Eq. (31).

$$S_{\text{cells}}(t) = \frac{\phi_u^{s,\text{abs}}(t) A_{pv} \eta_{pv}}{V_{pv}} \tag{31}$$

where $\phi_u^{s,\text{abs}}(t) = (1 - \rho_{\text{front}})\phi_u^s(t)$ with $\rho_{\text{front}} = 0.05$ the reflectivity of the front side of the PV panel (selected according to [8]). The solar flux generally corresponds to the global horizontal radiation or the radiation in the plane of incidence of the panel. In the model presented here, $\phi_u^s(t)$ corresponds to the incident flux density in the plane of the PV panel.

The term η_{pv} is the effective electrical efficiency of the cells and linearly depends on their temperature (Eq. (32)).

$$\eta_{pv} = \eta_{\text{ref}} \left[1 - \beta_{\text{ref}}(T(\mathbf{x}, t) - T_{\text{ref}})\right] \tag{32}$$

In Eq. (32), the reference efficiency of the panel ($\eta_{\text{ref}} = 18.86\,\%$) and the cell temperature coefficient ($\beta_{\text{ref}} = 0.004\,\text{K}^{-1}$) are given by the manufacturer. The reference temperature T_{ref} is the temperature at STC, i.e. 25 °C.

2.3.3. Sky temperature modeling

The boundary conditions are radiative and convective in nature and take place mainly on the front and back sides of the panel. On the front face, the incident solar flux and the radiative exchange with the sky are taken into account. The back face exchanges with the air by convection and by radiation with the ground at temperature T_{ground}. This temperature can also be modeled or taken as an input. In most models, the ground temperature is considered to be equal to the ambient temperature. Sky temperature (T_{sky}) is a concept that is particularly used in building simulations. The temperature of the outer space is close to absolute zero but because of the atmosphere with different gases, particles and water vapor the fictive sky temperature is greater. Therefore, this sky temperature depends on cloud cover, relative humidity, pollution and so on. The literature is quite extensive on modeling the sky temperature as a function of these different atmospheric conditions, location, etc. These models can be direct by using the air temperature only or indirect by first calculating a sky emissivity and then applying the usual radiative formula of the radiative flux to derive the sky temperature [35]. For the direct models, two equations are commonly used when there is no cloud cover (Eqs. (33) and (34)) which corresponds to clear sky conditions. Conversely, Eq. (35) is more appropriate for significant cloud cover (cloudy sky conditions).

$$T_{\text{sky}} = T_{\text{air}} - 20 \tag{33}$$

$$T_{\text{sky}} = 0.0552\, T_{\text{air}}^{1,5} \tag{34}$$

$$T_{\text{sky}} = T_{\text{air}} - 6 \tag{35}$$

However, if the downward longwave flux $\phi_{LW}^{\downarrow}$ is available, it is possible to directly calculate the sky temperature using Eq. (36).

$$T_{\text{sky}} = \left(\frac{\phi_{LW}^{\downarrow}}{\sigma_{\text{SB}}}\right)^{\frac{1}{4}} \tag{36}$$

In Eqs. (33)–(36), temperatures are given in Kelvin. The temperature difference between the panel and the ambient temperature is relatively small so we proceed to a linearization of the radiative transfers through a coefficient h_{rad} in order to use the radiative path described in Section 2.1.2. This coefficient is calculated for the radiative transfers between the panel and the sky as well as between the panel and the ground.

2.3.4. Modeling convective heat transfer

Convective heat transfer coefficients are calculated for natural (h_{cvn}) and forced (h_{cvf}) convections. The literature presents a large number of correlations to calculate these coefficients from the scaled Rayleigh (Ra), Reynolds (Re) and Prandtl (Pr) numbers. The correlations used for natural and forced convection are given by Eqs. (37) and (38) respectively.

$$\text{Nu}_{\text{cvn}} = \begin{cases} 0.76\,\text{Ra}^{1/4} & \text{if} \quad 10^4 < \text{Ra} < 10^7 \\ 0.15\,\text{Ra}^{1/3} & \text{if} \quad 10^7 < \text{Ra} < 3 \times 10^{10} \end{cases} \tag{37}$$

$$\text{Nu}_{\text{cvf}} = 0.86\,\text{Re}^{1/2}\text{Pr}^{1/3} \tag{38}$$

The convective heat transfer coefficients are then calculated from the Nusselt number knowing that $h_{cv} = \frac{\text{Nu} k_{\text{air}}}{L_c}$ where k_{air} is the conductivity of air (W m^{-1} K^{-1}) and L_c the characteristic length of the PV panel (m).

For convective transfers, the film temperature (see Eq. (39)) has to be computed to get the corresponding thermophysical properties of air. To avoid iterative calls between the main algorithm which solves for the panel temperature and the convective heat transfers, an estimate of the surface temperature is used. The formula given by King et al. [36] (see Eq. (40)) was used and provides a rather good estimate of the surface temperature for the back sheet.

$$T_{\text{film}} = \frac{T_{\text{air}} + T_{\text{surf}}}{2} \tag{39}$$

where T_{surf} is the surface temperature of the PV panel.

$$T_{\text{estimate}} = T_{\text{air}} + \phi_{\text{poa}} \exp(a + b(V)) \tag{40}$$

where ϕ_{poa} is the plane of array irradiance (POA), V is the wind speed, $a = -3.56$ and $b(V) = -0.0750$ for the open configuration of the PV panel (Eq. (40)).

2.3.5. Modeling cell aging

The simulations presented above take place over relatively short operating periods and do not include the effect of cell aging during their lifetime [37]. This topic is well known to panel manufacturers and indeed most of them provide aging laws in their datasheets. Most of the time, the datasheets present linear decreases of the electrical efficiency with time. In the case of the studied panel, the efficiency level is considered to go no lower than 97 % of the initial efficiency during the first two years of operation. From the third year, the output drops by 0.65 % each year. After 25 years of operation, the yield is 81.40 % of the initial electrical output. This data is incorporated into the model for simulations running over long periods.

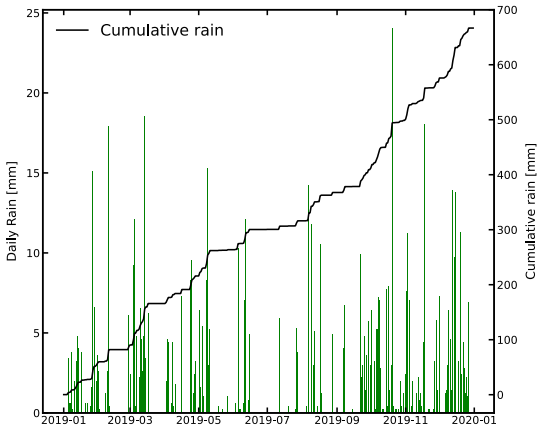

(a) Rainfall events in Nancy in 2019 and cumulative rain.

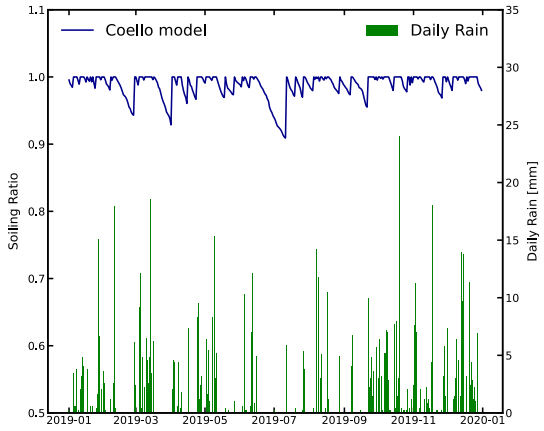

(b) Rainfall (green line) an soiling ratio simulation from Coello's model (blue line)

Fig. 5. Soiling ratio simulated from Coello's model. The cleaning ratio is set to 0.3 mm d^{-1} for soiling ratio. This value is chosen according to the literature [39].

The decrease in the PV's efficiency is given in Eq. (41).

$$\eta_{\text{ref}}(t) = 0.97 \times (1 - \alpha t) \tag{41}$$

where $\alpha = 0.65\%$ and t is the time in years and starts from $t = 3$.

2.3.6. *Modeling of soiling and cleaning of the PV panel*

A panel is negatively affected by its operating temperature and many studies focus on this issue as was explained in the introduction. However, weather conditions can cause other parasitic effects on the electrical production. Among these effects, an important issue is the deposition of dust on the panel, which causes a significant decrease in electrical production due to the solar mask it creates.

Several models exist in the literature to describe the amount of particles deposited on the surface of a photovoltaic panel over time. The periods of particle deposition are interspersed with periods of natural (rain events) or mechanical cleaning [38]. Among the existing models, those based on Particle Matter (PM) quantities seem to be the most suitable. The input data of these models are PM10, PM2.5, wind speed and ambient temperature. The application of a dust deposition model allows the amount of particles deposited in grams per square meter to be extracted in fine. Then, a soiling ratio (SR) is derived and applied to the incident solar radiation in the plane of array. When there is no particle deposition, the soiling ratio is equal to unity whereas a soiling ratio equal to zero means the PV panel is completely covered with dust.

In this study, the Coello model proven to provide good results [39] was used. This model is based on a theory that is common to most soiling models and some details are presented below.

The soiling process on the panel is the result of the deposition, rebound and resuspension of the material particles. In general, the models used do not distinguish between these three processes and only a deposition velocity is calculated as in Eq. (42).

$$v_d = \frac{1}{r_a + r_b} + v_s \tag{42}$$

where r_a is the aerodynamic resistance, r_b is the quasilaminar resistance and v_s is the settling velocity.

The aerodynamic resistance depends on the meteorological parameters such as wind speed and air temperature and is calculated as in Eq. (43).

$$r_a = \frac{1}{C_D U} \tag{43}$$

where C_D is the surface drag coefficient and U the wind speed measured at the reference height z_{ref}.

The quasi-laminar resistance r_b is calculated using the friction velocity (Eq. (44)) and the Schmidt number. This resistance describes the flow exchanges in the laminar sublayer corresponding to a limit between the perfectly mixed fluid far from the surface and the fluid close to the surface where a no-slip condition is applied.

$$u^\star = \frac{\kappa U}{\ln\left(\frac{z_{\text{ref}}}{z_0}\right)} \tag{44}$$

where $\kappa = 0.41$ is the von Karman constant and z_0 is the surface roughness fixed at 1 m.

To compute the settling velocity (see Eq. (45)), the Reynolds number is assumed to be less than 1 for all particles (PM10 and PM2.5).

$$v_s = \frac{\rho_p g d_p^2}{18\mu} \tag{45}$$

where ρ_p is the particle density, g is the gravitational constant, d_p is the particle diameter (respectively 10 µm for PM10 and 2.5 µm for PM2.5).

According to [40], the mass accumulation in kg m^{-2} on the PV panel at each time step is given by Eq. (46).

$$m = (v_{10-2.5} C_{10-2.5} + v_{2.5} C_{2.5}) \cos(\theta) t \tag{46}$$

where $v_{10-2.5}$ (resp. $v_{2.5}$) is the deposition velocities for PM10 (resp. PM2.5), $C_{10-2.5}$ (resp. $C_{2.5}$) is the particle concentration for PM10 (resp. PM2.5), θ is the tilt angle of the PV panel and t is the time step in seconds (hourly or daily).

At each time step, the quantity m is added to the total mass deposition w to obtain the cumulative mass. Finally, the soiling ratio is calculated using Eq. (47). When a rainfall event occurs and the threshold value (3 mm in the present study) is exceeded, the total mass deposition w is reset to zero.

$$\text{SR}(t) = 1 - 0.3437 \operatorname{erf}(0.17 w^{0.8473}) \tag{47}$$

where t is the time step for the soiling ratio. In the result section, the soiling ratio (SR) will be pre-calculated from the weather data as an input to the model with a daily time step.

Two locations will be studied in the result section. The first will be Nancy in France because the experimental work from this study took place there. The second place was chosen in the state of Nevada (USA) near to Las Vegas where one of the biggest photovoltaic installations is located. It also interesting to compare these two locations with reference to the Köppen climate classification [41]. According to this classification, Nancy (France) is *Cfb* which corresponds to a *temperate oceanic climate* whereas Las Vegas (USA) is *Bwk* which stands for *cold desert climate*. Therefore, the two selected sites should lead to different results and interesting complementary analyses. The data for the US location are taken from the United States Environmental Protection

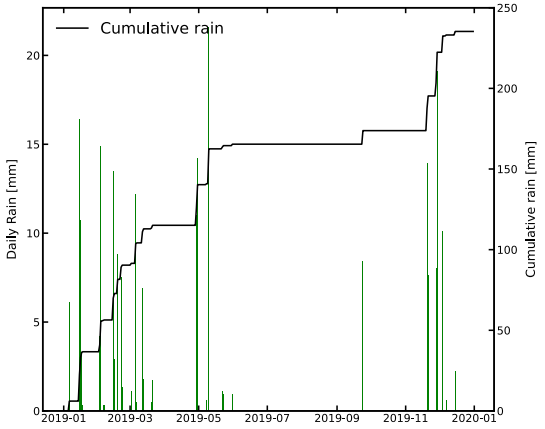

(a) Rainfall events in Nevada in 2019 and cumulative rain.

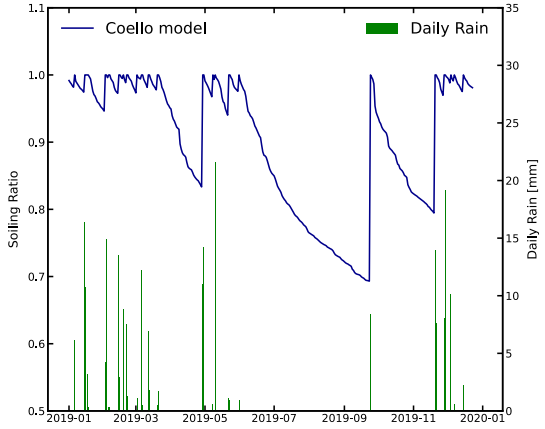

(b) Rainfall (green line) an soiling ratio simulation from Coello's model (blue line)

Fig. 6. Soiling ratio simulated from Coello's model. The cleaning ratio is set to 0.3 mm d^{-1} for soiling ratio. This value is chosen according to the literature [39].

Agency.[1] For France, the online portal Geodair was used.[2] The reason for having chosen these two very different locations can be seen in the representation of the precipitation and the simulated soiling ratio (see Figs. 5 to 6). In the Nevada region rainfall is very low and the desert environment favors the deposit of dust on the panel. As there is almost no precipitation from mid-June to mid-September in Nevada, the soiling ratio has been observed to go down to 0.7. In comparison, the year 2019 in Nancy is relatively typical and therefore quite rainy which leads to a much more constant soiling ratio that does not go below 0.91.

2.3.7. *Time integration: estimation of the electrical production*

For time-integrated simulations, the objective is to obtain the energy produced by a photovoltaic panel over long periods of time without omitting events that appear dynamically in the energy balance. Then, the electrical production found by the current model is compared to the production predicted by the PVGIS tool.[3] This tool is capable of predicting the electrical production for a given location over a year with monthly details. Firstly, the current model was applied to June 2022 in Nancy using the local weather data whereas PVGIS uses satellite data. Secondly, the energy is estimated for a whole year (2019) using weather data from the NREL laboratory as inputs of the presented model.

The electrical production (energy) is obtained by integrating the electrical power over time from t_{start} to t_{end}. In the formula of the power, the back side temperature was used. The other parameters are the meteorological variables (solar irradiance, wind speed, air, sky and ground temperatures) and the PV panel parameters from its datasheet.

The production is given in Eq. (48).

$$\begin{aligned} E_{\text{elec}} &= \int_{t_{\text{start}}}^{t_{\text{end}}} \mathrm{d}\tau \mathcal{P}_{\text{elec}}(\tau) \\ &= \int_{t_{\text{start}}}^{t_{\text{end}}} \mathrm{d}\tau \eta_{\text{ref}} \left[1 - \beta_{\text{ref}}(T_{\text{pv,cells}}(\tau) - T_{\text{ref}})\right] \mathrm{SR}(\tau) \phi_u^{s,\text{abs}}(\tau) A_{pv} \end{aligned} \tag{48}$$

where $\mathcal{P}_{\text{elec}}$ is the electrical power and $\mathrm{SR}(\tau)$ is the soiling ratio between 0 (maximum soiling) and 1 (no soiling) determined according to Eq. (47) and used as an input of the simulation.

The Eq. (48) can be expressed from a probabilistic point of view by the introduction of a probability density function over the time variable.

$$\begin{aligned} E_{\text{elec}} &= \int_{t_{\text{start}}}^{t_{\text{end}}} \mathrm{d}\tau p_{\mathcal{T}}(\tau) \left[\frac{\eta_{\text{ref}} \left[1 - \beta_{\text{ref}}(T_{\text{pv,cells}}(\tau) - T_{\text{ref}})\right] \mathrm{SR} \phi_u^{s,\text{abs}}(\tau) A_{pv}}{p_{\mathcal{T}}(\tau)} \right] \\ &= \mathbb{E}[\mathcal{E}] \end{aligned} \tag{49}$$

where $\mathcal{E}$ is the random variable of the electrical production. Once again, the double randomization was used for the Monte Carlo algorithm because the expectation of $\mathcal{E}$ is a function of $\mathbb{E}\left[T_{\text{pv,cells}}(\tau)\right]$. The corresponding algorithm is described in Algorithm 3.

$$\mathcal{E} = \mathbb{E}\left[\frac{\eta_{\text{ref}} \left[1 - \beta_{\text{ref}}(\mathbb{E}\left[T_{\text{pv,cells}}(\tau)\right] - T_{\text{ref}})\right] \mathrm{SR}(t) \phi_u^{s,\text{abs}}(\tau) A_{pv}}{p_{\mathcal{T}}(\tau)} \right] \tag{50}$$

Algorithm 3: Description of the Monte Carlo algorithm to estimate the electrical production

```
Sample τ according to p_T
Initialize t = τ
if φ_u^s(τ) = 0 then
    w = 0
else
    Evaluate T_pv,cells(τ) according to Algorithm 1 and Algorithm 2
    w = η_ref[1−β_ref(T_pv,cells−T_ref)]SR(τ)φ_u^s,abs(τ)A_pv / p_T(τ)
```

It has to be noted that the probability density function (PDF) $p_{\mathcal{T}}$ can be chosen arbitrarily. A uniform probability density function was chosen as a first approach. This means that the times are sampled uniformly between t_{start} and t_{end} (see Eq. (51)). This choice is obviously not optimal because the selected times will be sampled indifferently at night or during the day. However, the electricity production is zero at night, thus the number of realizations must be increased to obtain a suitable standard deviation (lower than 1 kWh for example).

$$p_{\mathcal{T}}(\tau) = \frac{1}{t_{\text{end}} - t_{\text{start}}} \tag{51}$$

Implementing the algorithm with this uniform time sampling requires about one million realizations to achieve this standard deviation. Even if the calculation time remains small for this number of realizations on a personal computer (only a few minutes), it is interesting to optimize the number of realizations necessary to obtain the same standard deviation which implies to optimize the PDF function. For that purpose, a new PDF function is introduced using the distribution of the

[1] https://www.epa.gov/pm-pollution

[2] https://www.geodair.fr/

[3] PVGIS: https://joint-research-centre.ec.europa.eu/pvgis-photovoltaic-geographical-information-system_en.

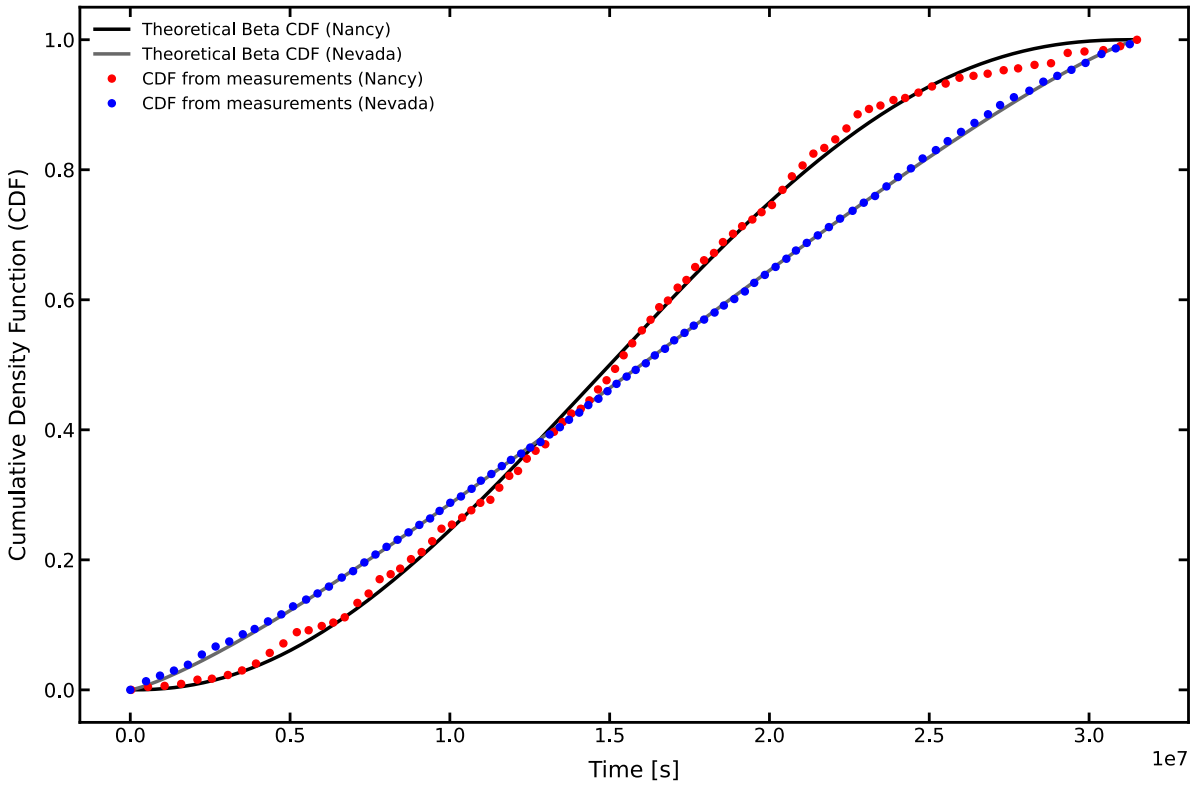

Fig. 7. Cumulative density function (CDF) of the plane of array irradiance with respect to time over 2019 year for Nancy and Nevada.

incident radiation values at the panel in Eq. (52).

$$p_{\mathcal{T}}(\tau) = \frac{\phi_u^{\text{abs}}(\tau)}{\int_{t_{\text{start}}}^{t_{\text{end}}} \mathrm{d}t' \phi_u^{\text{abs}}(t')} \tag{52}$$

The cumulative distributions of solar irradiance with respect to time during 2019 is showed in Fig. 7 for the Nancy and Nevada locations. Only the non-null values of solar irradiance are kept to construct the CDF. These distributions demonstrate a typical beta distribution as it is highlighted by the fitted beta cumulative density function (CDF) whose equation is given in Eq. (53). For the case of Nevada, the CDF is very close to that of a uniform distribution because the solar radiation is well distributed throughout the year which is not the case in Nancy. For both cases, the CDF from the solar irradiance data is numerically inverted and interpolated to sample the times according to this distribution.

$$f(x, \alpha, \beta) = \frac{\Gamma(\alpha + \beta)}{\Gamma(\alpha)\Gamma(\beta)} x^{\alpha-1}(1-x)^{\beta-1} \tag{53}$$

where $\alpha > 0$, $\beta > 0$ are parameters of the distribution, $0 < x < 1$ and Γ is the gamma function.

The new expression of the energy production estimate is given in Eq. (54).

$$E_{\text{elec}} = \int_{t_{\text{start}}}^{t_{\text{end}}} \mathrm{d}\tau p_{\mathcal{T}}(\tau) \mathcal{H}(\phi_u^{\text{abs}}(\tau) > 0) w \tag{54}$$

where $w = \eta_{\text{ref}} \left[1 - \beta_{\text{ref}}(T_{\text{pv,cells}}(\tau) - T_{\text{ref}})\right] \text{SR}(\tau) A_{pv} \int_{t_{\text{start}}}^{t_{\text{end}}} \mathrm{d}t' \phi_u^{\text{abs}}(t')$ is the Monte Carlo weight.

3. Results and discussion

3.1. Studied photovoltaic panel and experimental platform

The modeled system is a monocrystalline photovoltaic panel (Recom-Sillia Series 60M) of 310 W composed of 60 cells in series and whose dimensions were 1660 × 990 × 4.45 mm. The main parameters of the PV panel are described in Table 2. The thickness of the panel is broken down into five layers - a layer of glass in front (3 mm), a first layer of EVA (0.45 mm), the silicon photovoltaic cells (0.15 mm), a second layer of EVA (0.45 mm) and of a polymer back face (0.4 mm). The configuration of the platform with the PV panel is shown in Fig. 9.

3.2. Validation in controlled conditions

For the validation in controlled conditions a complete description of the experimental setup and the different sensors are presented in our previous work [42]. One of the experiments carried out in this previous study consisted in the illumination of the PV panel with an artificial light and the observation of the panel's thermal behavior for period of time with electrical production and non-production. These experiments resulted in the construction of line plots with the time evolution of the back panel temperature for different ambient temperatures in the room. In the present study, the results for a typical 25 °C ambient temperature were extracted and used as validation test case for the developed model. The PV panel efficiency measurements in these experimental conditions were also used as input parameters for the model. The convective transfers were essentially natural because the air speed in the controlled room was very low (about 0.4 m s^{-1}). In the model, the values of the front and back sides convective coefficients were set at 4.2 W m^{-2} K^{-1} and 3.8 W m^{-2} K^{-1} respectively. Taking into account the radiative transfer coefficients after linearization, the resulting exchange coefficient is of the same order of magnitude as those determined in [42]. Finally, the model was used to simulate the backside temperature of the PV panel. The results of the simulation are shown in Fig. 8 and demonstrate a good fit between the simulation and the measurements. The RMSE is 0.88 °C. For this simulation, the number of Monte Carlo realizations for each point of the graph is 20×10^4. This test case is also of interest to check that the model behaves well with the thermal parameters described in Table 1.

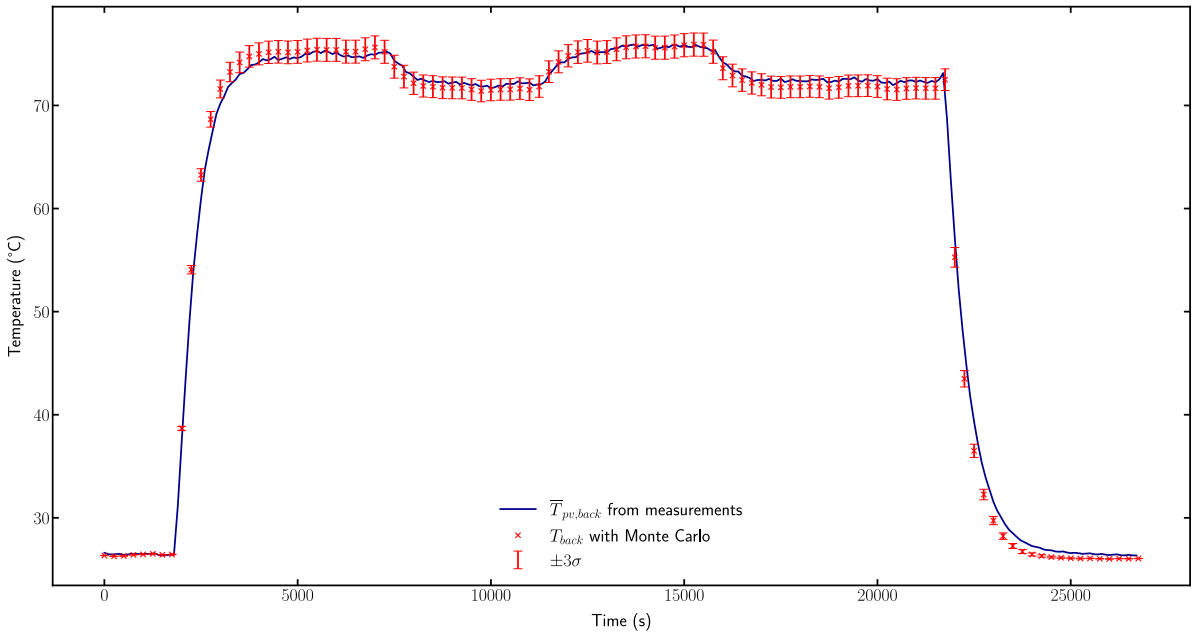

Fig. 8. Simulation of the temperature on the back side of the panel and comparison with experimental measurements obtained at controlled room temperature. The number of realizations for the Monte Carlo simulation is 20×10^4 per time point.

Table 2
Main parameters of the Recom-Sillia photovoltaic panel.

Electrical parameters at *STC*	60M310
Cells	Monocrystalline Silicon
Power at MPP	310 W
Module Efficiency	18.86 %
Voltage at MPP	32.35 V
Current at MPP	9.56 A
Open circuit Voltage	39.60 V
Short circuit Current	9.95 A
Pmax Temperature Coefficient	−0.40 %/°C

3.3. Validation in real conditions

After having validated the model under controlled conditions, we now need to move on to a validation in real operating conditions. For this purpose, the measurements from a gravel roof are used and the model is applied to simulate the temperature at the center of the backside of the PV panel. This kind of roof limits the transfer of water types and is a good representation of the vast majority of rooftop photovoltaic installations. The real configuration is shown in Fig. 9.

Fig. 9. 310 W photovoltaic panel used in the present study in a gravel platform. The pyranometer is in the plane of array of the panel and the pyrometer is pointing under the PV panel. The other sensors are hidden by the PV panel.

3.3.1. Day 1: Summer day with clear sky conditions

The first simulation in outdoor conditions was carried out on July-18-2022 corresponding to a perfect summer day without clouds. The meteorological parameters are displayed in Fig. 10(a). The corresponding results from the Monte Carlo simulations for PV panel temperature at the center of the backside and the DC power output are presented in Fig. 10(b).

The RMSE value is 0.96 °C which demonstrates a good fit between the simulated and the experimental temperatures. The largest temperature difference occurs around noon when the PV panel reaches its highest temperature. This gap can be attributed to an increase in convective exchanges by natural convection which may be underestimated by the correlation used (see Eq. (37)).

3.3.2. Day 2: Summer day with cloudy sky conditions

June 6 2022 was chosen for the second validation. It was another summer day but with a very cloudy sky as can be seen in Fig. 11(a) with plane of array irradiance measurements. The corresponding results from the Monte Carlo simulations for PV panel temperature at the center of the backside and the DC power output are presented in Fig. 11(b). In these meteorological conditions, the fluctuations of the backside temperature are very large but are well captured by the model as is displayed in Fig. 11(b). The RMSE is only 0.74 °C for these cloudy conditions.

3.3.3. Day 3: Summer day with rain conditions

The aim of this configuration is to test the robustness of the model in rainy conditions with a significant level of evaporation from the soil. This term is not directly taken into account in the energy balance of the PV panel and could cause deviation between simulated and measured temperatures. The selected day is June 26 2022 when several rain events occurred and the day's meteorological parameters are shown in Fig. 12(a). The corresponding results from the Monte Carlo simulations

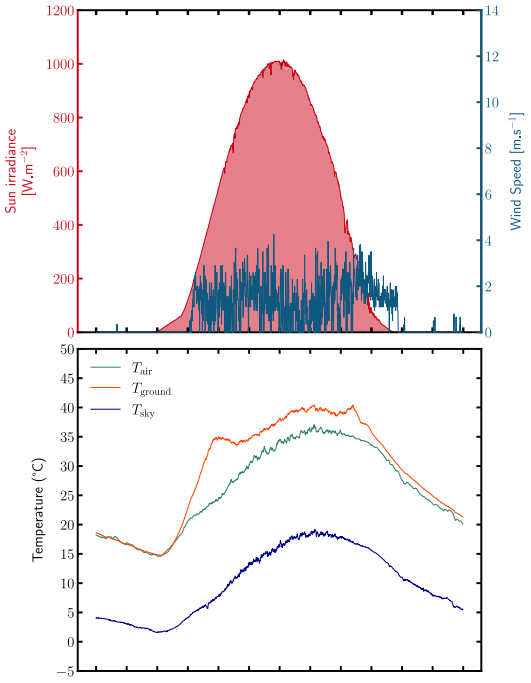

(a) Weather data for clear sky conditions (Day 1)

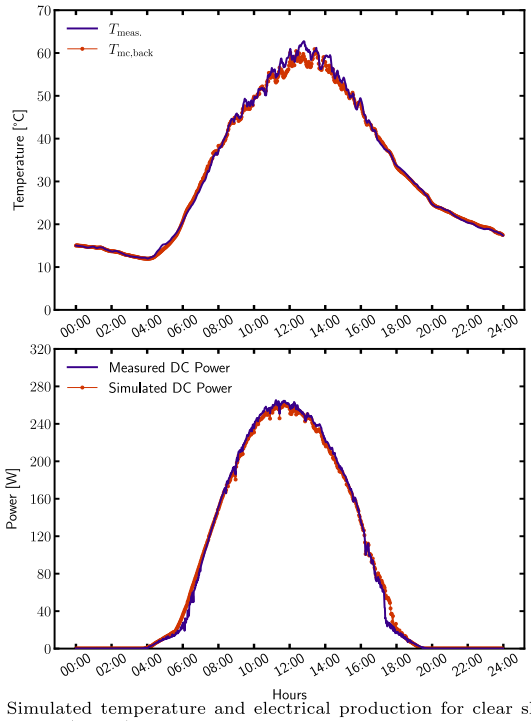

(b) Simulated temperature and electrical production for clear sky conditions (Day 1)

Fig. 10. Monte Carlo simulations for clear sky conditions (Day 1). The temperature of the PV panel is simulated at the center of the backside with 20×10^4 realizations and compared with measurements.

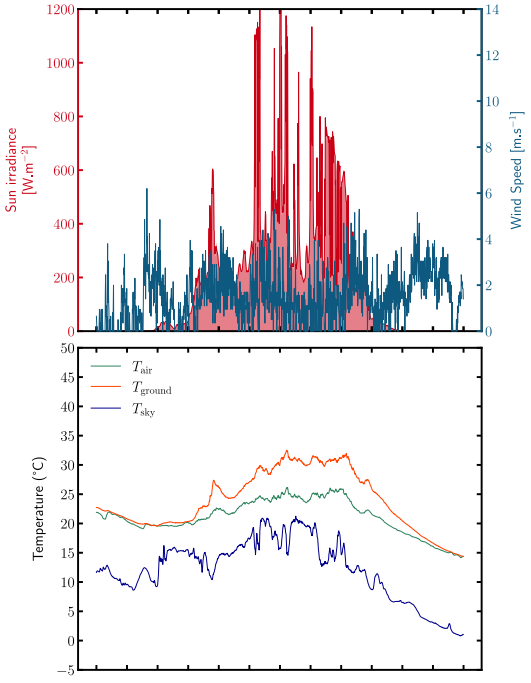

(a) Weather data for cloudy conditions (Day 2)

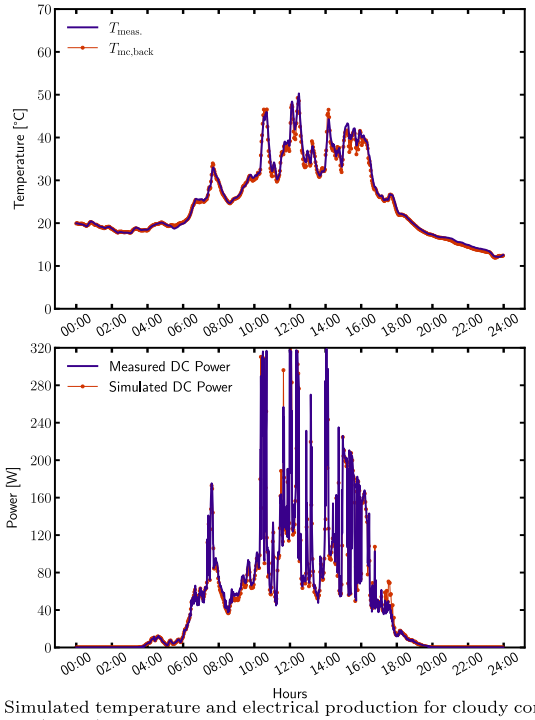

(b) Simulated temperature and electrical production for cloudy conditions (Day 2)

Fig. 11. Monte Carlo simulations for cloudy conditions (Day 2). The temperature of the PV panel is simulated at the center of the backside with 20×10^4 realizations and compared with measurements.

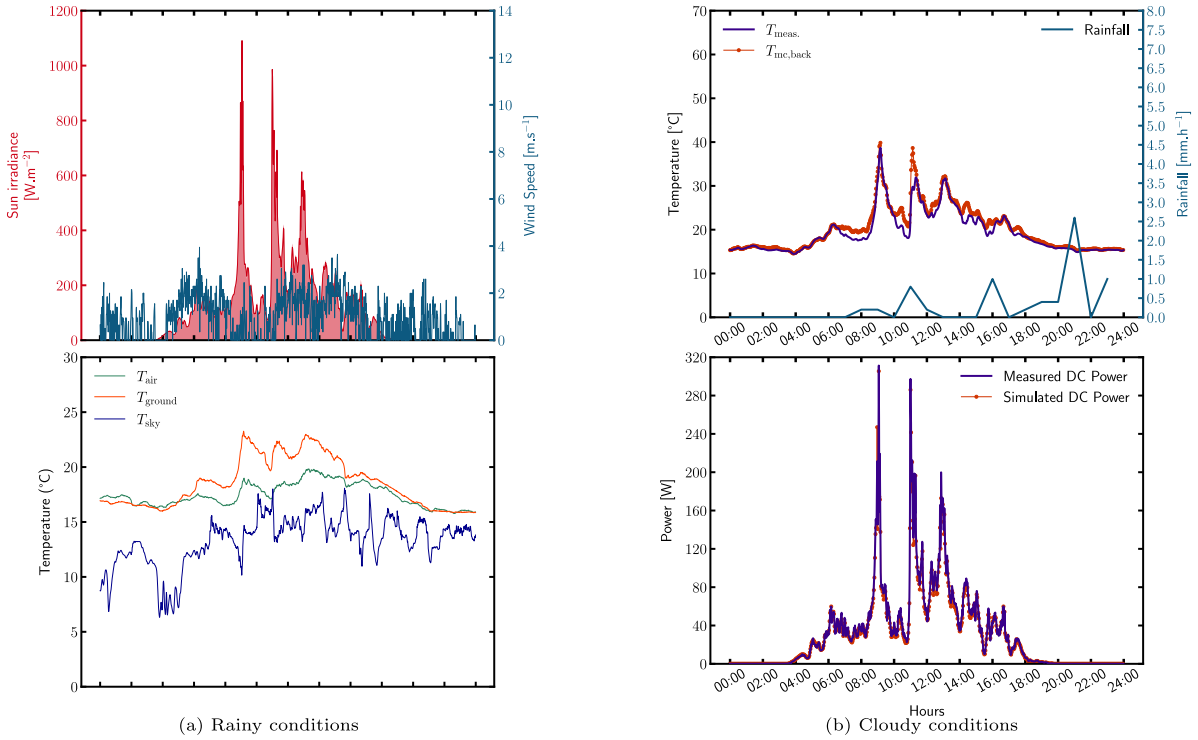

(a) Rainy conditions (b) Cloudy conditions

Fig. 12. Monte Carlo simulations for rainy conditions (Day 3). The temperature of the PV panel is simulated at the center of the backside with 20×10^4 realizations and compared with measurements.

for PV panel temperature at the center of the backside and the DC power output are presented in Fig. 12(b) and rainfall are superimposed on the temperature graph.

As expected, an overestimation of the panel temperature at precipitation times is well observed and the RMSE for this rainy day is 1.41°. The difference between the measurements and the simulation remains acceptable and the electrical production is expected to be low at these times. However, study of these rainy events in the thermal model could more usefully be the subject of a separate work with direct reference to other studies in the literature on active cooling ([43] for instance). However, it is interesting to note that even with this difference between the simulated and measured temperatures, the estimate of instantaneous electrical production is very close to that measured using the experimental instrumentation.

3.4. Time integration: estimation of the annual electrical production

In this section, the electrical production is assessed at different time scales, first of all on a monthly basis for the month of June 2022 where experimental data are available, then on an annual basis and over several years where the Monte Carlo model is compared with PVGIS results.

3.4.1. Electrical production for june 2022

June 2022 is chosen to compare the measured electrical power to the estimated energy productions from the current model and PVGIS tool. The data are collected from the local weather station and used as inputs for the model.

The data shows that the measured DC energy production from the experimental platform is 51.26 kWh. From the Monte Carlo simulations, the estimated energy without soiling is 51.1 ± 0.33 kWh and 50.7 ± 0.33 kWh with activation of the soiling. These results are also compared with those from the PVGIS tool. With the same location, tilt angle, azimuthal orientation and mounting configuration, PVGIS estimates the AC electrical production for a typical June month to be 40.45 kWh.

The DC/AC efficiency of the micro-inverter installed on the Cerema facilities is 97 % according to the datasheet. Therefore, the Monte Carlo estimate is 49.6 ± 0.33 kWh (resp. 49.2 ± 0.32 kWh) without soiling (resp. with soiling). From the Enphase manager tool, the AC production for June 2022 is 47.7 kWh.

In conclusion, the results obtained with the model for the DC electrical production are in very good agreement with the experimental measurements. A difference of about 1.5 kWh is observed when converting to AC current. This discrepancy could derive from several sources, particularly the measurement on the AC side which could take into account electricity consumed in part by the acquisition system (about 2 kWh per month) or the losses in the cables linking the micro-inverter to the AC acquisition unit (Envoy from the Enphase company). The differences observed between the estimates obtained by our model and PVGIS can have several explanations. Firstly, the input data are not the same. PVGIS uses satellite data, whereas in our June assessment, local data were used for the Monte Carlo model. Local data provide a more accurate estimate, as they are closer to actual weather conditions at PV panel level. This is reinforced by the particular architecture of the building on which the photovoltaic panel is installed. Indeed, PVGIS allows to choose the type of mounting as Building Integrated, but does not fully reflect the actual mounting. In addition, PVGIS does not estimate production on the DC side, but on the AC side of the installation. Even though the DC/AC conversion has been calculated based on the efficiency of the microinverter, this may introduce an additional bias into the comparison of the two results. Finally, the thermal model used by PVGIS to evaluate the PV panel temperature is a function of the irradiance, air temperature and wind speed and does not take into account the thermal capacity of the PV panel [44,45].

3.4.2. Annual production and monthly analysis

The aim is to estimate the energy produced over a year by a 310 W PV panel located in Nancy (France) and the same PV panel near Las Vegas (Nevada, United States) where one of the biggest photovoltaic plants is installed. These two locations present very different weather and solar conditions and should provide very different results for the

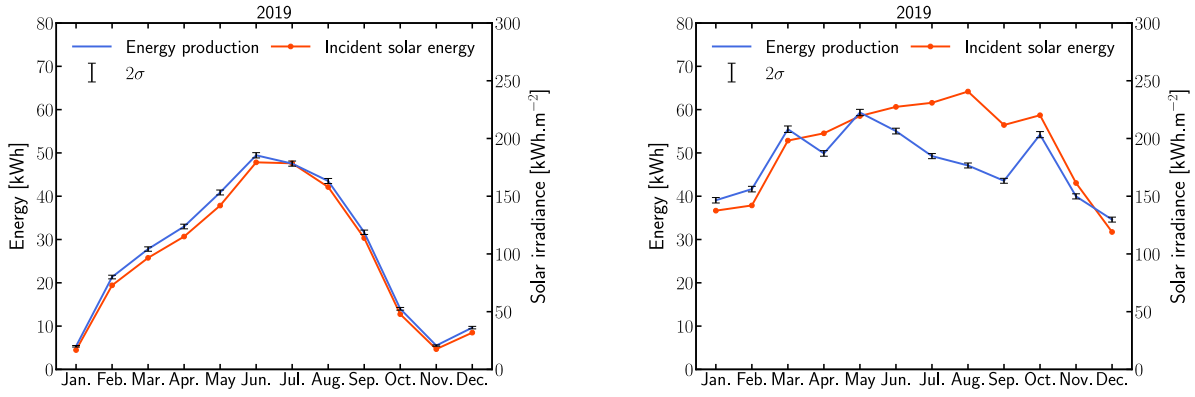

(a) Nancy in 2019

(b) Nevada in 2019

Fig. 13. Monthly photovoltaic production compared to monthly solar energy for Nancy and Nevada locations in 2019. Graphically, the photovoltaic production is above the incident solar energy for most months except July, August and September. This observation is characteristic of the negative effect of temperature on the electrical production during the summer period.

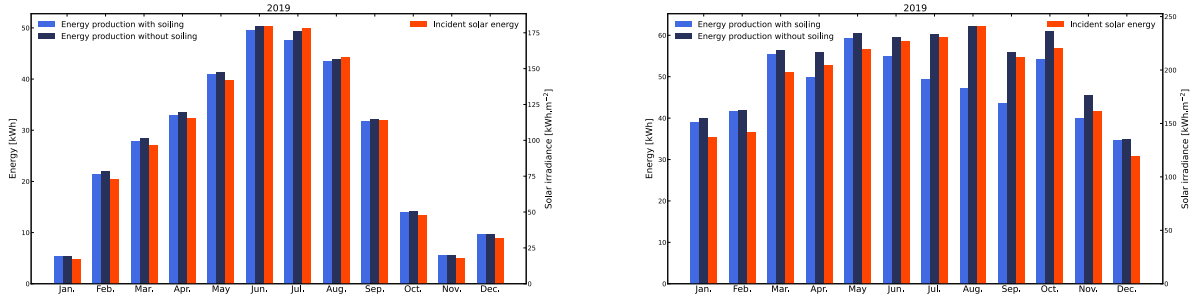

(a) Nancy in 2019

(b) Nevada in 2019

Fig. 14. Comparison of the results for Nancy and Las Vegas with and without soiling ratio activated.

electrical production. For this longer time period, the 2019 weather data from the NREL laboratory were used. The global, diffuse and direct horizontal irradiances were extracted from the data file to calculate the plane of array (POA) irradiance of a 30° tilted and south-oriented PV panel. Air temperature and wind speed were also used from the NREL file. The soiling ratio was calculated using rainfall events measured from the local weather station. The long-wave radiation data were not available in the data file and Eq. (34) was used to calculate the sky temperature from air temperature.

Using the CDF described in Eq. (52) and plotted in Fig. 7 to estimate the annual energy production in Nancy, only 10,000 realizations are necessary to achieve a standard deviation of 0.89 kWh which means that the number of realizations has been reduced by a factor of 100 compared to the previous uniform PDF. The same comments apply to the location in Nevada even though the solar irradiation is well distributed over 2019. The use of preferential sampling is very efficient for the two selected locations.

The current model estimates the annual electrical production at 329.1 kWh with a standard deviation equal to 0.43 kWh with soiling ratio activated. For the same situation without soiling the energy production is higher and reaches 335 kWh with a standard deviation equal to 0.44 kWh. Considering a conversion factor equal to 0.97 (which corresponds to the DC/AC efficiency of the Enphase IQ7+ micro inverter) from DC to AC, the annual energy production is 319.23 kWh for the soiling case and 325 kWh without soiling. The annual production estimated by the PVGIS tool is 334.86 kWh with a year-to-year variability equal to 17.34 kWh (the mounting configuration chosen is *Building integrated*). This comparison with PVGIS provides an initial indication of the order of magnitude expected for electricity production over a year under these weather conditions. Obviously, the two models are not intended to give the same indications. PVGIS aims to quantify the photovoltaic potential of an installation at a given location whereas the present model aims to describe more precisely the physical mechanisms at play between the PV panel and its environment, in order to obtain a more accurate estimate. It can be deduced from the results shown above that Monte Carlo is able to predict the annual energy production from a PV panel without over simplification of the heat transfers involved in the thermal balance of the system. In addition, the model presented could be improved to include transfers that are still ignored as it is the case for the mass transfers.

For the case of the PV panel located in Nevada, the same kind of simulations were carried out. The annual electrical production with soiling is 569.5 kWh with a standard deviation of 0.82 kWh. Without soiling, the energy output is estimated at 633.5 kWh with a standard deviation equal to 0.82 kWh. As expected, the PV panel placed in Nevada produces about twice as much as the one placed in Nancy because the radiation received in Nancy is about twice as low (2429.37 kWh near Las Vegas and 1237.92 kWh at Nancy). Monthly photovoltaic prodution and monthly solar energy are shown in Fig. 13 for Nancy and Nevada locations. Another interesting result is the effect of soiling on the Nevada panel where there is much less rain which results in long periods of dust deposition (see Fig. 14).

The effect of soiling is quite small at the Nancy site with only 6 kWh difference between the two simulations. This can be explained by the high levels and frequency of rain at this location. On the other hand, the effect is very marked for the panel in Nevada, with a very sharp drop in production in July, August and September. In these regions, the deposition of dust at the scale of the photovoltaic plant

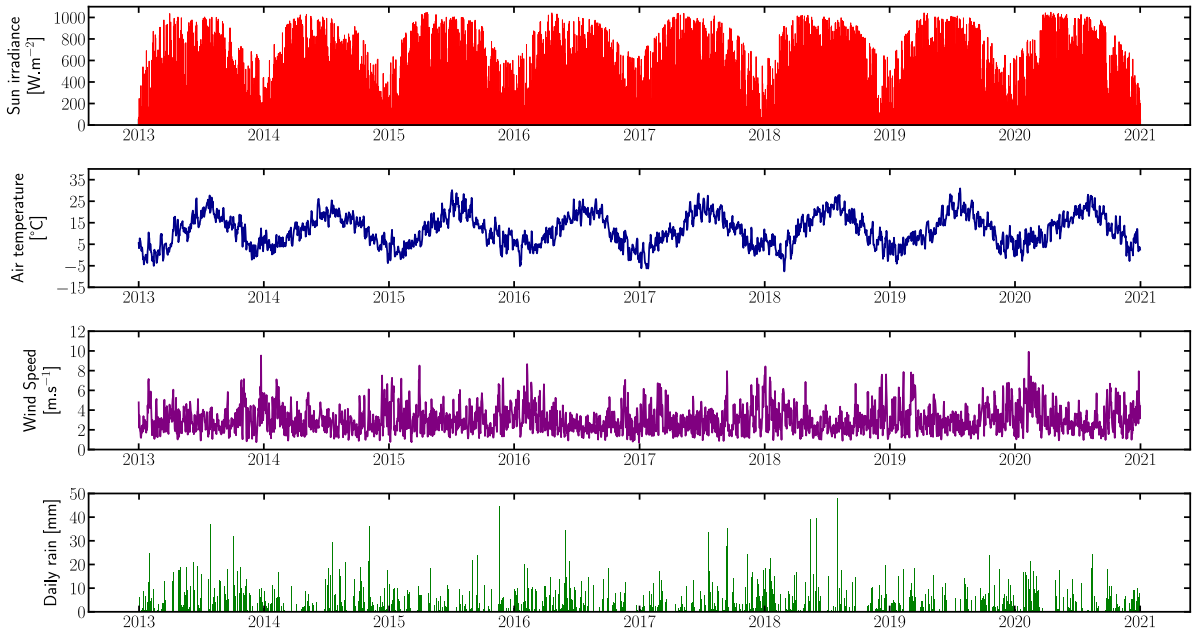

Fig. 15. Weather data for the simulation of the electrical production over eight years in Nancy.

could be a significant issue because the summer months are often marked by this type of episode without rainfall [46]. In this case, the photovoltaic panel is working in a very degraded configuration in which low precipitation events do not permit the natural recovery of the optimal electrical production capacities.

3.4.3. Electrical production over several years

In this last section the electrical production of the panel is evaluated over an eight-year period from 2013 to 2020 in Nancy. The meteorological data presented in Fig. 15 come from Meteo-France and the particle data are extracted from the same source as in Section 3.4.2. It is possible to obtain an estimate of the electrical production with only 10,000 Monte Carlo realizations by integrating soiling and aging effects on the PV panel with a standard deviation around 10 kWh thanks to double randomization.

With soiling and aging effects activated, the electrical production over the eight years is 3159.8 kWh with a standard deviation equal to 10.8 kWh. Without the aging effect, the electrical output for the same period is 3336.9 kWh with a standard deviation equal to 11.4 kWh. Therefore, the production would be 5 % greater without cell degradation from January 2013 to December 2020.

The simulation is carried out for only 8 years as we have no data for particle matter prior to 2013 for the site under study (Nancy). Extending the simulation to a longer period of time using simulated data (e.g. from a General Circulation Model used for climate change modeling and climate forecasting with the aim of optimal plant design issues) is feasible within the same calculation time which is only 7 s for 10000 realizations in this configuration. Therefore, it is quite possible to evaluate the electrical production of the panel in a realistic environment by keeping the input meteorological data at a very fine time step while keeping the calculation time constant.

From a numerical point of view, it is worth noting that the double randomization process makes it possible to sequence several integrals without significantly increasing CPU time. Indeed, the time required for the Monte Carlo algorithm to converge depends mainly on the most complex integral which, in the present work, is not the integral over time. This method is particularly efficient in this framework and this property has already been demonstrated in [30,47].

4. Future work and applications

Several perspectives are envisaged following this work. Firstly, instead of using experimental data for panel surface temperature, it is possible to model heat transfers within the building using a Monte Carlo approach. An application of building-scale heat transfers has already been implemented. In this work, the aim was to obtain an estimate of the building's heating and cooling energy requirements. Several configurations were studied, with or without the presence of a photovoltaic field. The ultimate goal is to couple the two models to estimate the energy needs, including the electrical energy produced by the photovoltaic field on the roof. In a second step, several parametric studies can be carried out to find optimums for building orientation, wall thickness and so on. Other applications at city-sized scales using more complex geometries may be the subject of future work. Coupling such a model with airflow calculation codes for complex geometries would then be necessary. Another perspective of this work is to develop an electrical model of the active component (the PV cell) in the framework of the Monte Carlo method.

5. Conclusions

In this work, a 3D model of the heat balance of a 310 watt photovoltaic panel was developed, solved using the Monte Carlo method and validated under controlled and real conditions. The demonstrated benefits of this path space formulation are renewed physical images and insensitivity of computation times to the dimension of the integration domain (here to the number of coupled phenomena and the time period) and to the geometrical complexity at all scales. To validate the model in real conditions, several days with different weather conditions were extracted and exploited to determine the backside temperature of the panel. The results were compared with measurements taken on a panel in real conditions on a gravel platform. The results obtained demonstrate the ability of the model to reproduce the temperature at the back of the panel even if the model has some limitations. For example, it does not account for mass transfers that could occur between the PV panel and the environment, especially for rainfall events, condensation and evaporation phenomena. In addition, the convective transfer is modeled through convective coefficients based

on correlations. It could be possible to take into account the convective transfer with the Monte Carlo method in future works.

Then, the model was used to determine electrical production over longer time periods: first during the month of June 2022 to compare with on site experimental data, then for a year (2019) for two very different locations – Nancy and near Las Vegas – to highlight the practicality of the model at larger time scales and finally over 8 years from 2013 to 2020 in Nancy alone. The simulations also included soiling and aging effects for this longer time period. Soiling was demonstrated to sometimes have a very significant negative effect in some regions of the world if no cleaning is planned.

For these longer simulations, the results were compared with PVGIS tool to demonstrate that the model can produce very reliable results. The graphs of monthly energies enabled the temperature effect to be highlighted even in a temperate region like Nancy. Finally, the model was optimized to take into account the solar distribution over the chosen locations and the number of realizations need for Monte Carlo was divided by a factor of 100. This is a very promising and valuable result for the present model because the end goal of the model is to evaluate the electrical production over several years – typically 25 – to analyze the effect of passive cooling techniques on the output energy.

Funding

This research work was carried out within the scope of the PROOF Project, funded by the French National Research Agency (ANR) under the grant number no ANR-19-CE22-008.

Declaration of competing interest

The authors declare that they have no known competing financial interests or personal relationships that could have appeared to influence the work reported in this paper.

Data availability

Data will be made available on request

Acknowledgments

The computational environment used in this study is based on the open source library Star-Engine developed by the start-up Meso-Star (https://www.meso-star.com/projects/misc/about-fr.html).

This work was carried out using HPC resources from the University of Lorraine's EXPLOR Mesocentre (https://explor.univ-lorraine.fr/).

The authors would like to thank the Recom-Sillia and Enphase companies for donating equipment for this study.

References

[1] Irena, 2020, https://irena.org/solar.

[2] G.N. Tiwari, R.K. Mishra, S.C. Solanki, Photovoltaic modules and their applications: A review on thermal modelling, Appl. Energy 88 (7) (2011) 2287–2304, http://dx.doi.org/10.1016/j.apenergy.2011.01.005, URL https://www.sciencedirect.com/science/article/pii/S0306261911000080.

[3] NREL, 2022, https://www.nrel.gov/pv/cell-efficiency.html.

[4] L. Xu, W. Liu, H. Liu, C. Ke, M. Wang, C. Zhang, E. Aydin, M. Al-Aswad, K. Kotsovos, I. Gereige, A. Al-Saggaf, A. Jamal, X. Yang, P. Wang, F. Laquai, T.G. Allen, S. De Wolf, Heat generation and mitigation in silicon solar cells and modules, Joule 5 (3) (2021) 631–645, http://dx.doi.org/10.1016/j.joule.2021.01.012, URL https://www.sciencedirect.com/science/article/pii/S254243512100043X.

[5] S. Dubey, J.N. Sarvaiya, B. Seshadri, Temperature dependent photovoltaic (PV) efficiency and its effect on PV production in the world – A review, Energy Procedia 33 (2013) 311–321, http://dx.doi.org/10.1016/j.egypro.2013.05.072, URL https://www.sciencedirect.com/science/article/pii/S1876610213000829.

[6] Y. Du, C.J. Fell, B. Duck, D. Chen, K. Liffman, Y. Zhang, M. Gu, Y. Zhu, Evaluation of photovoltaic panel temperature in realistic scenarios, Energy Convers. Manage. 108 (2016) 60–67, http://dx.doi.org/10.1016/j.enconman.2015.10.065, URL https://www.sciencedirect.com/science/article/pii/S0196890415009875.

[7] D. Moser, M. Pichler, M. Nikolaeva-Dimitrova, Filtering procedures for reliable outdoor temperature coefficients in different photovoltaic technologies, J. Sol. Energy Eng. 136 (2) (2014).

[8] S.P. Aly, S. Ahzi, N. Barth, A. Abdallah, Using energy balance method to study the thermal behavior of PV panels under time-varying field conditions, Energy Convers. Manag. 175 (2018) 246–262, http://dx.doi.org/10.1016/j.enconman.2018.09.007, URL https://www.sciencedirect.com/science/article/pii/S0196890418310033.

[9] S. Nižetić, A. Papadopoulos, E. Giama, Comprehensive analysis and general economic-environmental evaluation of cooling techniques for photovoltaic panels, part I: Passive cooling techniques, Energy Convers. Manage. 149 (2017) 334–354, http://dx.doi.org/10.1016/j.enconman.2017.07.022, URL https://www.sciencedirect.com/science/article/pii/S019689041730657X.

[10] S. Nižetić, M. Jurčević, D. Čoko, M. Arıcı, A novel and effective passive cooling strategy for photovoltaic panel, Renew. Sustain. Energy Rev. 145 (2021) 111164, http://dx.doi.org/10.1016/j.rser.2021.111164, URL https://www.sciencedirect.com/science/article/pii/S1364032121004536.

[11] N. Gilmore, V. Timchenko, C. Menictas, Microchannel cooling of concentrator photovoltaics: A review, Renew. Sustain. Energy Rev. 90 (2018) 1041–1059, http://dx.doi.org/10.1016/j.rser.2018.04.010, URL https://www.sciencedirect.com/science/article/pii/S1364032118302193.

[12] D. Sato, N. Yamada, Review of photovoltaic module cooling methods and performance evaluation of the radiative cooling method, Renew. Sustain. Energy Rev. 104 (2019) 151–166.

[13] R. Li, Y. Shi, M. Wu, S. Hong, P. Wang, Photovoltaic panel cooling by atmospheric water sorption–evaporation cycle, Nat. Sustain. 3 (8) (2020) 636–643.

[14] E. Skoplaki, J.A. Palyvos, On the temperature dependence of photovoltaic module electrical performance: A review of efficiency/power correlations, Sol. Energy 83 (5) (2009) 614–624, http://dx.doi.org/10.1016/j.solener.2008.10.008, URL https://www.sciencedirect.com/science/article/pii/S0038092X08002788.

[15] A.G. Gaglia, S. Lykoudis, A.A. Argiriou, C.A. Balaras, E. Dialynas, Energy efficiency of PV panels under real outdoor conditions–An experimental assessment in Athens, Greece, Renew. Energy 101 (2017) 236–243, http://dx.doi.org/10.1016/j.renene.2016.08.051, URL http://www.sciencedirect.com/science/article/pii/S0960148116307522.

[16] A.R. Jatoi, S.R. Samo, A.Q. Jakhrani, An improved empirical model for estimation of temperature effect on performance of photovoltaic modules, Int. J. Photoenergy 2019 (2019).

[17] E. Skoplaki, A. Boudouvis, J. Palyvos, A simple correlation for the operating temperature of photovoltaic modules of arbitrary mounting, Sol. Energy Mater. Sol. Cells 92 (11) (2008) 1393–1402.

[18] L. de Oliveira Santos, P.C.M. de Carvalho, C. de Oliveira Carvalho Filho, Photovoltaic cell operating temperature models: A review of correlations and parameters, IEEE J. Photovolt. (2021).

[19] O. Dupré, R. Vaillon, M.A. Green, Thermal behavior of photovoltaic devices, Phys. Eng. 10 (2017) 978–3.

[20] G. Notton, C. Cristofari, M. Mattei, P. Poggi, Modelling of a double-glass photovoltaic module using finite differences, Appl. Therm. Eng. 25 (17) (2005) 2854–2877.

[21] J. Zhou, Q. Yi, Y. Wang, Z. Ye, Temperature distribution of photovoltaic module based on finite element simulation, Sol. Energy 111 (2015) 97–103.

[22] R. Santbergen, C. Rindt, H. Zondag, R.C. Van Zolingen, Detailed analysis of the energy yield of systems with covered sheet-and-tube PVT collectors, Sol. Energy 84 (5) (2010) 867–878.

[23] S. Armstrong, W.G. Hurley, A thermal model for photovoltaic panels under varying atmospheric conditions, Appl. Therm. Eng. 30 (11) (2010) 1488–1495, http://dx.doi.org/10.1016/j.applthermaleng.2010.03.012, URL http://www.sciencedirect.com/science/article/pii/S1359431110001225.

[24] A.D. Jones, C.P. Underwood, A thermal model for photovoltaic systems, Sol. Energy 70 (4) (2001) 349–359, http://dx.doi.org/10.1016/S0038-092X(00)00149-3, URL http://www.sciencedirect.com/science/article/pii/S0038092X00001493.

[25] SANDIA, 2022, https://pvpmc.sandia.gov/.

[26] J. Kim, M. Rabelo, S.P. Padi, H. Yousuf, E.-C. Cho, J. Yi, A review of the degradation of photovoltaic modules for life expectancy, Energies 14 (14) (2021) 4278.

[27] S.P. Aly, S. Ahzi, N. Barth, Effect of physical and environmental factors on the performance of a photovoltaic panel, Sol. Energy Mater. Sol. Cells 200 (2019) 109948, http://dx.doi.org/10.1016/j.solmat.2019.109948, URL https://www.sciencedirect.com/science/article/pii/S0927024819302776.

[28] N. Villefranque, F. Hourdin, S. Blanco, O. Boucher, C. Caliot, C. Coustet, J. Dauchet, M. El-Hafi, V. Eymet, O. Farges, V. Forest, R. Fournier, J. Gautrais, V. Masson, B. Piaud, R. Schoetter, The "teapot in a city": A paradigm shift in urban climate modeling, Sci. Adv. 8 (27) (2022) http://dx.doi.org/10.1126/sciadv.abp8934, URL https://hal-mines-albi.archives-ouvertes.fr/hal-03718009.

[29] M. Sans, O. Farges, V. Schick, G. Parent, Solving transient coupled conductive and radiative transfers in porous media with a Monte Carlo Method: Characterization of thermal conductivity of foams using a numerical Flash Method, Int. J. Therm. Sci. 179 (2022) 107656.

[30] O. Farges, J.-J. Bézian, H. Bru, M. El Hafi, R. Fournier, C. Spiesser, Lifetime integration using Monte Carlo Methods when optimizing the design of concentrated solar power plants, Sol. Energy 113 (2015) 57–62.

[31] J.M. Tregan, J.L. Amestoy, M. Bati, J.-J. Bézian, S. Blanco, L. Brunel, C. Caliot, J. Charon, J.-F. Cornet, C. Coustet, L. D'alençon, J. Dauchet, S. Dutour, S. Eibner, M. El-Hafi, V. Eymet, O. Farges, V. Forest, R. Fournier, L. Ibarrart, M. Galtier, V. Gattepaille, J. Gautrais, P. Lavieille, Z. HE, F. Hourdin, J.-L. Joly, P. Lapeyre, M.-H. Lecureux, J. Lluc, M. Miscevic, N. Mourtaday, Y. Nyffenegger-Péré, L. Pelissier, L. Penazzi, B. Piaud, C. Rodrigues-Viguier, G. Roques, M. Roger, T. Saez, G. Terrée, N. Villefranque, T. Vourc'h, D. Yaacoub, Coupling radiative, conductive and convective heat-transfers in a single Monte Carlo algorithm: A general theoretical framework for linear situations, PLoS One 18 (4) (2023) http://dx.doi.org/10.1371/journal.pone.0283681, URL https://imt-mines-albi.hal.science/hal-04066139.

[32] S. Maire, G. Nguyen, Stochastic finite differences for elliptic diffusion equations in stratified domains, Math. Comput. Simulation 121 (nil) (2016) 146–165, http://dx.doi.org/10.1016/j.matcom.2015.09.008.

[33] S. Maire, G. Nguyen, Stochastic finite differences for elliptic diffusion equations in stratified domains, Math. Comput. Simulation 121 (2016) 146–165.

[34] M. Bossy, N. Champagnat, H. Leman, S. Maire, L. Violeau, M. Yvinec, Monte Carlo methods for linear and non-linear Poisson-Boltzmann equation, ESAIM: Proc. Surv. 48 (2015) 420–446.

[35] L. Evangelisti, C. Guattari, F. Asdrubali, On the sky temperature models and their influence on buildings energy performance: A critical review, Energy Build. 183 (2019) 607–625.

[36] D.L. King, J.A. Kratochvil, W.E. Boyson, Photovoltaic Array Performance Model, United States. Department of Energy, 2004.

[37] T. Rahman, A. Al Mansur, S. Islam, M.I. Islam, M. Sahin, M.R. Awal, A. Shihavuddin, M.A.U. Haq, Effects of aging factors on PV modules output power: An experimental investigation, in: 2022 4th International Conference on Sustainable Technologies for Industry 4.0, STI, IEEE, 2022, pp. 1–5.

[38] G. Osma-Pinto, G. Ordóñez-Plata, Dynamic thermal modelling for the prediction of the operating temperature of a PV panel with an integrated cooling system, Renew. Energy 152 (2020) 1041–1054.

[39] J.G. Bessa, L. Micheli, J. Montes-Romero, F. Almonacid, E.F. Fernández, Estimation of photovoltaic soiling using environmental parameters: A comparative analysis of existing models, Adv. Sustain. Syst. 6 (5) (2022) 2100335.

[40] M. Coello, L. Boyle, Simple model for predicting time series soiling of photovoltaic panels, IEEE J. Photovolt. 9 (5) (2019) 1382–1387.

[41] H.E. Beck, N.E. Zimmermann, T.R. McVicar, N. Vergopolan, A. Berg, E.F. Wood, Present and future Köppen-Geiger climate classification maps at 1-km resolution, Sci. Data 5 (1) (2018) 1–12.

[42] T. Villemin, R. Claverie, J.-P. Sawicki, G. Parent, Thermal characterization of a photovoltaic panel under controlled conditions, Renew. Energy 198 (2022) 28–40.

[43] G. Osma-Pinto, G. Ordóñez-Plata, Measuring factors influencing performance of rooftop PV panels in warm tropical climates, Sol. Energy 185 (March) (2019) 112–123, http://dx.doi.org/10.1016/j.solener.2019.04.053.

[44] D. Faiman, Assessing the outdoor operating temperature of photovoltaic modules, Prog. Photovolt., Res. Appl. 16 (4) (2008) 307–315.

[45] M. Koehl, M. Heck, S. Wiesmeier, J. Wirth, Modeling of the nominal operating cell temperature based on outdoor weathering, Sol. Energy Mater. Sol. Cells 95 (7) (2011) 1638–1646.

[46] A. Kimber, L. Mitchell, S. Nogradi, H. Wenger, The effect of soiling on large grid-connected photovoltaic systems in California and the southwest region of the United States, in: 2006 IEEE 4th World Conference on Photovoltaic Energy Conference, Vol. 2, IEEE, 2006, pp. 2391–2395.

[47] J. Dauchet, J.-J. Bézian, S. Blanco, C. Caliot, J. Charon, C. Coustet, M. El-Hafi, V. Eymet, O. Farges, V. Forest, R.A. Fournier, M. Galtier, J. Gautrais, A. Khuong, L. Pelissier, B. Piaud, M. Roger, G. Terrée, S. Weitz, Addressing nonlinearities in Monte Carlo, Sci. Rep. 8 (1) (2018) http://dx.doi.org/10.1038/s41598-018-31574-4, art.13302–11 p.URL https://imt-mines-albi.hal.science/hal-01871366.